

Yin Yang 1 and guanine quadruplexes protect dopaminergic neurons from cellular stress via transmissive dormancy

Received: 17 January 2024

Accepted: 25 November 2024

Published online: 04 December 2024



Kielen R. Zuurbier^{1,2}, Rene Solano Fonseca¹, Sonja L. B. Arneaud¹, Jordan M. Wall¹, Juhee Kim¹, Lexus Tatge¹, Gupse Otuzoglu¹, Sofia Bali^{2,3}, Patrick Metang¹ & Peter M. Douglas^{1,2,4}✉

Neurons deploy diverse adaptive strategies to ensure survival and neuro-transmission amid cellular stress. When these adaptive pathways are overwhelmed, functional impairment or neurodegeneration follows. Here we show that stressed neurons actively induce a state of transmissive dormancy as a protective measure. Extending observations of neurotrauma in *C. elegans* and mice, human dopaminergic neurons capable of surviving severe cellular challenges both decrease spontaneous activity and modulate dopamine homeostasis through the transcriptional regulator Yin Yang 1 (YY1). To bolster stress resilience and mitigate dopamine toxicity, YY1 increases expression of the vesicular monoamine transporter 2, vMAT2, while coordinately inhibiting dopamine synthesis through stabilization of a guanine quadruplex in intron 10 of tyrosine hydroxylase, TH. This dopaminergic stress response has the potential to cause circuit inactivation, yet safeguards neurons by minimizing the toxic accumulation of cytosolic dopamine and inducing a state of neuronal dormancy. In essence, neurons appear to actively prioritize viability over functionality.

Neurological disorders typically arise from neuronal cell death or loss of functionality, driven by factors such as genetic mutations, environmental influences, or the aging process. The manifestation of functional impairment often precedes the eventual demise of neurons^{1–4}. Various models of brain disease and spinal cord injury highlight the ability of neuronal circuitry to enter a dormant state while retaining the potential to be reactivated and regain functionality via electrical or optogenetic stimulation⁵. Yet the nature of transmissive dormancy remains unclear whether this represents a stochastic process rooted in dysfunction or a biologically significant and facilitated process employed by neurons. Throughout the body and brain, cells have developed an array of adaptive mechanisms known as stress response pathways. These pathways play a crucial role in sensing and

responding to diverse cellular stresses, both environmental or intrinsic, with the ultimate goal of restoring homeostasis and preserving cellular function. Due to their widespread presence across various cell types and their potential for therapeutic intervention, intracellular stress response pathways have garnered significant attention in the realm of neurodegenerative diseases. However, an intriguing question arises: when these foundational systems become overwhelmed, is it conceivable for neurons, as an auxiliary adaptive strategy, to initiate a state of transmissive dormancy for the purposes of ensuring their own long-term survival?

One documented neuronal subtype capable of stress-induced dormancy is dopaminergic neurons. These neurons have long been acknowledged for their heightened vulnerability to a diverse range of

¹Department of Molecular Biology; University of Texas Southwestern Medical Center, Dallas, TX 75390, USA. ²O'Donnell Brain Institute, UT Southwestern Medical Center, Dallas, TX 75390, USA. ³Center for Alzheimer's and Neurodegenerative Diseases, UT Southwestern Medical Center, Dallas, TX 75390, USA.

⁴Hamon Center for Regenerative Science and Medicine; UT Southwestern Medical Center, Dallas, TX 75390, USA.

✉ e-mail: peter.douglas@utsouthwestern.edu

stressors, a susceptibility often linked to inherent characteristics specific to dopaminergic function^{6–8}. Notably, they exhibit a high mitochondrial density, a critical feature essential for meeting their substantial energetic demands while concurrently managing the neurotoxic properties associated with the dopamine neurotransmitter^{9–11}. The hallmark of Parkinson's Disease lies in the dysfunction and demise of this specific neuronal subtype. The impairment of dopaminergic circuitry frequently precedes the degeneration of dopaminergic neurons in various Parkinson's Disease models, including those involving 6-hydroxydopamine injections⁵, mitochondrial poisons^{12,13}, genetic mitochondrial perturbations^{14,15}, α -synuclein overexpression¹⁶, administration of α -synuclein-preformed fibrils¹⁷, and the LRRK2(G2019S) mutation¹⁸. Additionally, a murine model of parkinsonism induced by impaired mitochondrial function showed a dramatic reduction of tyrosine hydroxylase (TH) protein levels at presynaptic terminals along the nigrostriatal circuit, which despite not being dead, corresponded with a loss in neurotransmission to the striatum¹⁵. Consistent observations indicate reduced dopaminergic firing rates, diminished dopamine synthesis, and subsequent synaptic release. Nevertheless, the question remains whether these observed changes are actively mediated or stem from passive dysfunction. Does this impairment contribute to the degeneration process or serve a protective role, and if so, is the adaptation in question mediated autonomously?

This study presents a thorough intracellular analysis elucidating the adaptive mechanisms employed by resilient dopaminergic neurons in the face of severe cellular stress. Surviving neurons actively recalibrate by reducing their intrinsic firing activity, minimizing dopamine synthesis, and enhancing the clearance of cytosolic dopamine. Orchestrated by the Yin Yang 1 (YY1) transcription factor, this adaptation appears focused on mitigating the inherent toxicity of cytosolic dopamine, a strategy aimed at prioritizing neuronal survival over immediate function. Our findings suggest the existence of a neuroprotective, YY1-mediated stress response tailored to dopaminergic neurons, triggered primarily by oxidative stress and DNA damage. Specifically, oxidative stress induces YY1-dependent transcriptional activation of the dopamine vesicular packaging gene, *SLC18A2*, through distal enhancer-binding. Concurrently, DNA damage prompts transcriptional repression of *TH*, through guanine quadruplex (G4) formation within intron 10 of the *TH* gene, followed by YY1 stabilization. Overall, we have identified YY1 as a pivotal regulator of a dopaminergic stress response (DSR), which mediates parallel modes of gene regulation with distinct kinetics, genomic binding elements, and molecular triggers. This not only implicates YY1 as a stress-responsive regulator of dopamine homeostasis but also positions it as a broader regulator of dopaminergic function and dormancy in a cellular stress-dependent fashion.

Results

Stress-resilient neurons actively compromise functionality

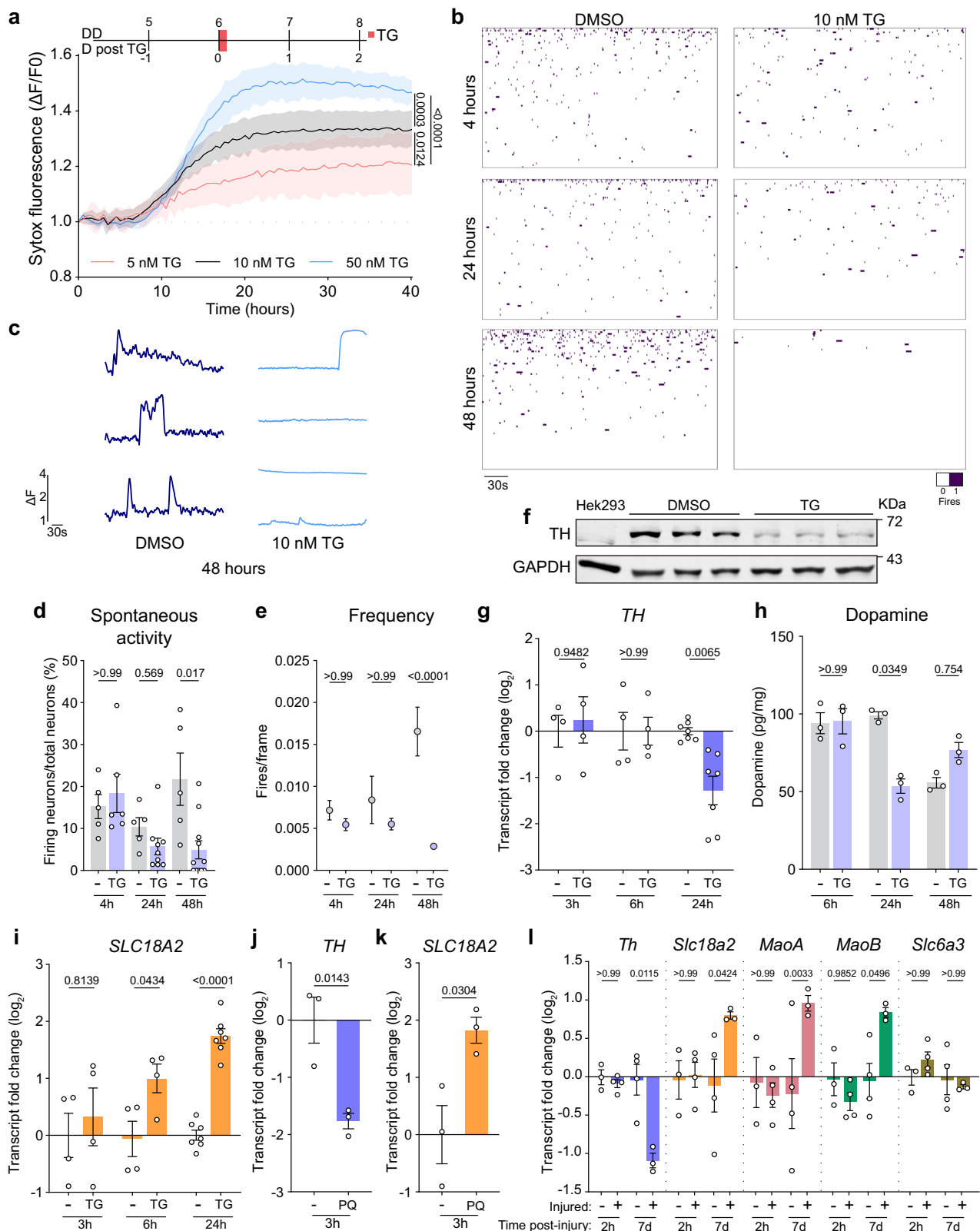
To examine the interplay between transmissive function and neuronal survival amid severe cellular stress, we established an in vitro model of stress-induced cell death of dopaminergic neurons. The objective of this model was to isolate a small subset of stress-resilient neurons and define the adaptive strategies used to ensure their viability. To this end, Lund's Human Mesencephalic Embryonic Stem (LUHMES) cells¹⁹, differentiated into postmitotic dopaminergic neurons, were stressed with thapsigargin (TG). TG causes broad cellular stress through irreversible blockade of the sarco-endoplasmic reticulum calcium ATPase (SERCA)²⁰. This inhibition of ER calcium uptake drives ER stress, while the increased cytosolic calcium promotes oxidative stress²¹, both broadly implicated in Parkinson's Disease pathogenesis^{6,22}. Treating LUHMES cells with a nanomolar range of TG led to dose-dependent apoptosis within 6–10 h without affecting HEK293t cells or normal human astrocyte (NHA) cell lines (Fig. 1a, Supplementary Fig. 1a–d). To study the resilient neurons that survive this stress, we opted for the

intermediate 10 nM TG concentration, which kills off ~67% of all neurons after 48 h (Supplementary Fig. 1e). We then assessed neuronal function in this resilient population via live-cell fluorescence imaging of the membrane permeable calcium indicator Fluo-4 AM. This revealed a significant reduction in neuronal activity 48 h post-TG, as evidenced by a reduction of neurons exhibiting spontaneous calcium transients and a lower firing frequency of the remaining active neurons (Fig. 1b–e, Supplementary Fig. 1f). Interestingly, TG treatment led to an increased firing amplitude at later timepoints which may be attributed to impaired calcium sequestration following depolarization (Supplementary Fig. 1g). Overall, these observations are consistent with in vivo mouse models of parkinsonism in which the dopaminergic neurons undergo a state of dormancy^{5,12–14,16–18,23,24}. Yet it remained unclear whether this reduction in neuronal activity was a proactive mechanism initiated by the neurons.

To better understand this, we performed genome-wide transcriptomics of LUHMES cells treated with TG and collected at timepoints (3-, 6-, and 24-hours post-TG) and identified 2082 differentially expressed genes (DEGs) (Supplementary Fig. 2a). As predicted, gene set enrichment analysis revealed upregulation of known intracellular stress response pathways across all timepoints including the integrated stress response and antioxidant defenses (Supplementary Fig. 2b–d). Yet more remarkably, DEGs downregulated 24 h post-TG were highly enriched for genes involved in neuronal function ranging from synapse assembly and organization to development and axon guidance (Supplementary Fig. 2d). No genes involved with cellular senescence were differentially expressed at any timepoint (Supplementary Fig. 3a) and established transcriptional markers of neuronal senescence (*CDKN1C*, *CDKN2A*, and *REST*)^{25,26} showed no induction upon TG supplementation (Supplementary Fig. 3b–d). This suggests that TG-driven impairment of neuronal function may be an actively regulated process that is distinct from established senescence pathways. Since cellular depolarization and re-establishing a membrane potential during action potentials come at a high energetic cost, perhaps these neurons reduce their activity to conserve energy.

Aside from spontaneous activity, it was unclear whether this impairment of neuronal function extended to synaptic potential and, more specifically, regulation of its neurotransmitter, dopamine. Mismanagement of dopamine synthesis, vesicular packaging, degradation, or synaptic reuptake is neurotoxic^{10,27–29}. More recently, we reported how dopamine toxicity is the determining factor underlying dopaminergic sensitivity to mechanical stress¹¹. Thus, controlling these dopamine-related processes could provide additional intracellular benefits for the neuron by enabling alternate means of stress adaptation. Indeed, TG treatment led to a significant reduction in TH transcripts, steady-state protein levels, and total dopamine concentration (Fig. 1f–h and Supplementary Fig. 4a, b). Despite the loss of TH expression being a widely used indicator of dopaminergic cell death, we observe stable expression of other dopaminergic markers, such as *SLC6A3/DAT1*, suggesting that reduced TH in this subset of resilient dopaminergic neurons is not the result of cell death (Supplementary Fig. 4c). In parallel to the reduction of dopamine synthesis, *SLC18A2* transcript levels were increased both 6- and 24-hours post-TG (Fig. 1i, Supplementary Fig. 4d). Due to the inverse regulation of *TH* and *SLC18A2* expression, this process is unlikely to be mediated through dopamine autoreceptor signaling which positively regulates both genes via CREB³⁰. Rather, due to the hyperreactivity of dopamine, we hypothesized that this transcriptional signature observed in LUHMES cells serves as a mode of intracellular adaptation that minimizes cytosolic dopamine oxidation and could mark the activation of a dopaminergic stress response (DSR).

Stress response pathways typically possess a molecular trigger that initiates a protective cell-wide response. Yet the molecular trigger responsible for DSR activation was unclear as TG causes both ER and oxidative stress. Thus, we asked if other non-ionic inducers of ER stress would repress *TH*. Rather than disrupting calcium fluctuations with TG,



we utilized tunicamycin as an alternate ER stress inducer, which disrupts core oligosaccharide conjugation to nascent polypeptides³¹. Contrary to TG, tunicamycin treatment did not repress *TH* but instead activated its transcription, suggesting that ER stress does not activate the DSR (Supplementary Fig. 4e). However, induction of oxidative stress via paraquat treatment was sufficient to both repress *TH* and activate *SLC18A2* (Fig. 1j, k). Intriguingly, paraquat activated this

regulation within 3 h, substantially faster compared to TG. Thus, oxidative stress appears to be a trigger for DSR activation downstream of calcium perturbations. Additionally, publicly available datasets of neural stem cells with a mutated form of the Parkinson's disease-related leucine-rich repeat kinase 2 (LRRK2 G2019S) and 3D bio-composite cultures of SH-SY5Y cells treated with MPP showed the same transcriptional signature (Supplementary Fig. 4f–h)^{32,33}.

Fig. 1 | Stress-resilient neurons actively repress neuronal function and dopamine synthesis. **a** SYTOX green fluorescence in LUHMES cells after a 30-minute thapsigargin (TG) pulse, ($\Delta F/F_0$). DD = days of differentiation, D post TG = days after TG removal. Brown-Forsythe and Welch one-way ANOVA with Dunnett's test using AUC. Mean \pm SEM. $n = 4$ replicates. **b** Binary firing plots of 80 most active LUHMES cells after TG treatment. Total time of acquisition = 5 min (350 frames). $n = 5$ for control and 5, 8, 11 for cells 4-, 24-, and 48-hours post-TG, respectively. **c** Representative traces of the most active neurons per individual recording. Fluo-4 AM fluorescence is normalized to the intrinsic minimum fluorescence per neuron (ΔF). **d** Percentage of neurons with spontaneous calcium transients. Ordinary one-way ANOVA with Šidák's correction. Mean \pm SEM. $n = 5$ for control and 5, 8, 11 for cells 4-, 24-, and 48-hours post-TG, respectively. **e** Frequency of neurons with spontaneous calcium transients. Recordings were collected at 1.16 Hz. Ordinary one-way

ANOVA with Šidák's correction. Mean \pm SEM. From left to right, $n = 124, 74, 80, 56, 62$, and 13. **f** TH protein levels in LUHMES cells 24 h after TG or vehicle treatment as determined by western blot. HEK293t cells serve as an anti-TH control in first lane. **g, i** qPCR quantification of *TH* and *SLC18A2* transcripts in LUHMES cells after TG treatment. Ordinary one-way ANOVA with Šidák's correction. Mean \pm SEM. $n = 4$ for 3- and 6-hours post-TG and $n = 7$ for 24-hours post-TG. **h** Dopamine content in LUHMES cells determined by ELISA after TG treatment. Kruskal-Wallis ANOVA with Dunn's correction. Mean \pm SEM. $n = 3$ replicates. **j, k** qPCR quantification of *TH* and *SLC18A2* transcripts in LUHMES cells treated with 100 μ M paraquat (PQ) for 3 h. Unpaired two-tailed t-test. Mean \pm SEM. $n = 3$ replicates. **l** Whole-brain RNA-seq collected 2 h and 7 days post-TBI in mice (GSE173431). Transcripts are normalized to time-matched uninjured controls. Ordinary one-way ANOVA with Šidák's correction. Mean \pm SEM. $n = 3$ for 2 h control and 7 d injury. $n = 4$ for 2 h injury and 7 d control.

We next sought to investigate whether DSR activation occurs in a more physiological context of dopaminergic stress. To this end, we assessed a mouse model of closed-head traumatic brain injury, which leads to nigrostriatal dopaminergic degeneration 28 days after injury³⁴. Consistent with the delayed repression of TH after intracellular stress of LUHMES cells, genome-wide transcriptomics revealed the same transcriptional signature of *Th* repression and *Slc18a2* induction seven days after injury, but this was not observed at the earlier 2-hour post-injury timepoint (Fig. 1l). Furthermore, the dopamine catabolizing enzymes, monoamine oxidase A and B (*MaoA/MaoB*), were both transcriptionally upregulated while the dopamine reuptake transporter, *Slc6a3*, remained unchanged. Thus, in addition to reducing dopamine synthesis and enhancing its vesicular packaging, dopaminergic neurons within the brain appear to accelerate the degradation of intracellular dopamine. These data provide further support that dopaminergic neurons alter dopamine homeostasis genes in an effort to minimize the toxic accumulation of cytosolic dopamine during times of cellular stress.

Cytosolic dopamine triggers an adaptive stress response

To further explore the molecular basis and conserved nature of this cell-type specific mechanism, we examined the nematode *C. elegans*, which possesses a simple nervous system with 302 neurons, including 8 dopaminergic neurons³⁵. We hypothesized that the DSR functions to minimize cytosolic dopamine and sought to determine whether increasing cytosolic dopamine levels would promote repression of dopamine synthesis. Transgenic worms that enable RNAi exclusively in dopaminergic neurons (XE1474 *dat-1p::rde-1::SL2::sid-1; rde-1(ne219)*) were fed double-stranded interfering RNAs targeting *cat-1*, the *C. elegans* orthologue of *SLC18A2*, thereby impairing the vesicular packaging of cytosolic dopamine. Transcriptional repression of the TH orthologue, *cat-2*, was observed in these worms raised on *cat-1/SLC18A2* RNAi (Fig. 2a).

While repression of *cat-2/TH* due to impaired dopamine packaging conforms to a stress response paradigm, it contradicts our understanding of the dopamine D2-autoreceptor negative feedback loop, which acts to ensure neurotransmission by restoring neurotransmitter production and release³⁰. Autoreceptor regulation would predict that decreased dopamine release after *cat-1/SLC18A2* RNAi would reduce autoreceptor activity and alleviate transcriptional repression of *cat-2/TH*, resulting in a net upregulation of *cat-2/TH* and dopamine production³⁰. Indeed, RNAi of the D2 dopamine receptor orthologue, *dop-2*, selectively in dopamine neurons caused *cat-2/TH* upregulation (Fig. 2b). However, co-administration of *dop-2* and *cat-1* RNAi negated this effect, suggesting that the transcriptional response to cytosolic dopamine accumulation overrides dopamine autoreceptor feedback.

Stress response pathways ensure cellular survival amid challenging conditions, and we sought to determine whether the DSR might serve a similar neuroprotective role. Utilizing our *C. elegans* model of mechanical stress, which promotes dopaminergic degeneration^{34,36},

we tested the physiological effects of DSR activation under stressful conditions. Transgenic worms, which were raised on *cat-1/SLC18A2* and subjected to blunt force trauma, retained significantly more GFP fluorescence in dopaminergic neurons 48 h after injury, indicating reduced dopaminergic cell loss since the neurons can maintain plasma membrane integrity^{36,37} (Fig. 2c). To corroborate these findings, we applied more temporal means of *cat-1/SLC18A2* inhibition. Treating animals with the irreversible *cat-1/SLC18A2* inhibitor, reserpine prior to injury also protected dopaminergic neurons from mechanical stress-induced degeneration (Fig. 2d), similar to pretreating the animals with *cat-1* RNAi. Preconditioning these animals with reserpine also prevented injury-induced formation of cytosolic oxidative stress as determined by the genetically encoded fluorescent peroxide sensor, ORP1-roGFP2, expressed within dopamine neurons¹¹ (Fig. 2e). Furthermore, similar effects were observed in LUHMES cells as reserpine pretreatment 24 h prior to the TG challenge resulted in significantly less cell death (Fig. 2f, Supplementary Fig. 5a, b). Yet, reserpine addition after TG treatment or prolonged high doses of reserpine both enhanced cell death (Fig. 2g, Supplementary Fig. 5a, b). Thus, cytosolic dopamine can mount an adaptive stress response in both *C. elegans* and human dopaminergic neurons, providing protection against subsequent stressors.

ZTF-17 regulates the dopaminergic stress response in *C. elegans*

We next sought to identify the transcriptional regulator of the DSR. Established regulators of dopamine homeostasis were dispensable for the stress-induced regulation of *cat-1/SLC18A2* (Supplementary Fig. 6a). Since free radical production via paraquat supplementation was sufficient to activate this response within 3 h, we reasoned that the molecular trigger sensed by the transcription factor was likely related to ROS formation. In further support, mice harboring a mutation in the mitochondrial cytochrome c oxidase assembly factor, SURF1, do not experience excessive mitochondrial superoxide production after traumatic brain injury³⁴ and failed to induce the DSR after traumatic brain injury (Fig. 3a). Thus, ROS appears both necessary and sufficient to trigger DSR activation. Leveraging these observations to identify the transcription factor required for DSR induction, we applied certain rational filtering criteria to generate a list of candidates (Supplementary Fig. 6b). First, we analyzed transcriptomic datasets from *Surf1*^{-/-} mice and selected transcription factors that exhibited differential regulation of downstream targets 7 days post-trauma in injured wildtype, but not in injured *Surf1*^{-/-} mice (Supplementary Fig. 5b). Second, candidate transcriptional regulators were further filtered based on selection criteria such as potential binding sites within the 5' promoter of *SLC18A2* (Supplementary Fig. 5c). Lastly, candidate transcription factors required conserved orthologues and documented expression in both human and worm dopamine neurons. Through this analytic pipeline, we narrowed our search to the cAMP response element-binding protein (CREB), heat shock factor 1 (HSF1), MYC, activating transcription factor 1 (ATF1), and Yin Yang 1 (YY1).

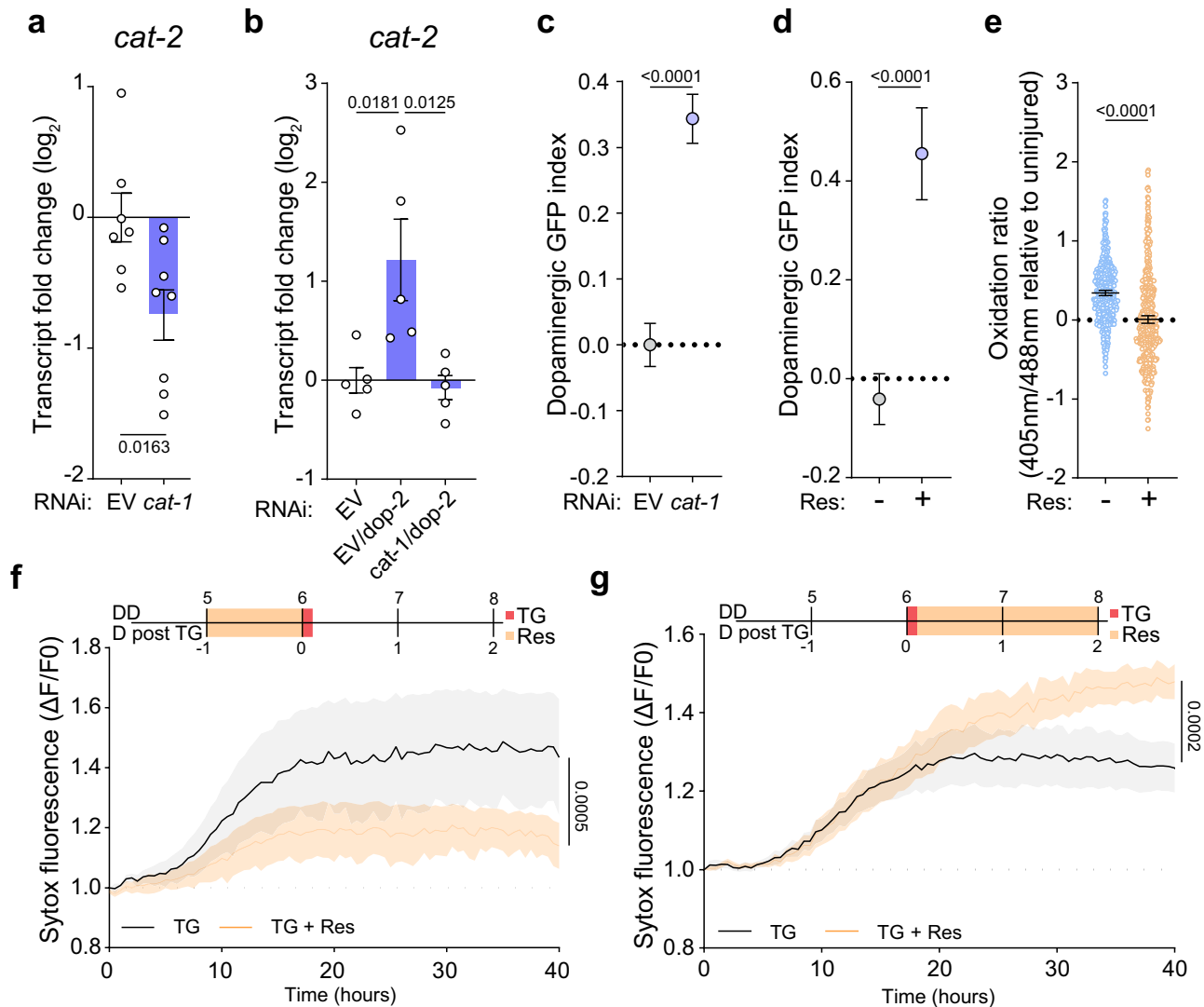


Fig. 2 | Cytosolic accumulation of dopamine triggers a neuroprotective dopaminergic stress response. **a** qPCR quantification of *cat-2/TH* in *C. elegans* (PMD216) raised on empty vector (EV) or *cat-1/SLC18A2* RNAi. Unpaired two-tailed t-test. Mean \pm SEM. $n = 8$ independent replicates. **b** qPCR quantification of *cat-2/TH* in *C. elegans* (PMD216) raised on EV, *dop-2/DRD2*, or 50/50 mixed *cat-1/dop-2* RNAi. Ordinary one-way ANOVA with Šidák's correction. Mean \pm SEM. $n = 5$ independent replicates. **c** Dopaminergic GFP retention in worms (PMD216) 48 h after injury. Positive and negative values show enhanced and reduced GFP retention respectively compared to injured EV control. Unpaired two-tailed t-test. Mean \pm 95% CI. From left to right, $n = 3696$ (EV), 3554 (*cat-1*) collected over 4 independent experiments. **d** Dopaminergic GFP retention in worms (PMD216) 48 h after injury, pretreated with 30 μ M reserpine (Res) or vehicle (acetic acid). Positive and negative values show enhanced and reduced GFP retention respectively compared to

injured vehicle. Unpaired two-tailed t-test. Mean \pm 95% CI. From left to right, $n = 1828$ and 1757 collected over 3 independent experiments. **e** Cytosolic ROS production in dopaminergic neurons 48 h after injury (PMD185). 405 nm/488 nm oxidation ratio is normalized to uninjured, time-matched, and vehicle control (acetic acid). Reserpine (Res) was supplemented to pre-injury agar plates at a final concentration of 30 μ M. Unpaired two-tailed t-test. Blue = injured and vehicle treated, beige = injured and reserpine pretreated. Mean \pm 95% CI. From left to right, $n = 485$ and 552 collected over 3 independent experiments. **f, g** SYTOX green fluorescence in LUHMES cells after a 10 nM TG pulse, ($\Delta F/F_0$). Cells were pretreated with 1 μ M reserpine prior to TG addition or treated with 10 μ M reserpine after TG removal. AUC was used for statistical analysis with an unpaired two-tailed t-test. DD = days of differentiation, D post TG = days post TG treatment. Mean \pm SEM. $n = 2$ independent replicates for (**f**) and $n = 7-8$ independent replicates for (**f**).

Utilizing the worm as an RNAi screening platform, we tested whether reduced expression of the closest, least divergent *C. elegans* orthologues as determined by Panther DB (pantherDB.org) prevented trauma-induced activation of *cat-1/SLC18A2*. As a positive control in the worm, RNAi against the cytochrome c oxidase subunit, *cox-5B*, was used to mimic the *Surf1*^{-/-} mice. From this candidate screen, both *mxl-2* and *ztf-17* were required for injury induced *cat-1/SLC18A2* transcription (Fig. 3b), and both RNAi treatments significantly worsened trauma-induced dopaminergic degeneration (Fig. 3c). However, only *ztf-17* was required for reserpine-mediated neuroprotection (Fig. 3d), and the combination of *ztf-17* RNAi and reserpine was sufficient to compromise dopaminergic GFP retention without injury (Fig. 3e).

Intriguingly, RNAi knockdown of *ztf-17* in dopaminergic neurons significantly increased cytosolic ROS levels by 164% ($\pm 15\%$) in dopaminergic neurons of healthy, uninjured animals without worsening the injury-induced ROS formation as indicated by ORP1-roGFP2 fluorescence quantification (Fig. 3f). Furthermore, co-administration of *cat-1/SLC18A2* and *ztf-17* RNAi in dopaminergic neurons resulted in upregulation of *cat-2/TH* compared to *cat-1/SLC18A2* RNAi alone (Fig. 3g), suggesting that *ztf-17* is required for the transcriptional repression of *cat-2/TH* upon inhibiting the vesicular packaging of dopamine. Transcriptional activation of *ztf-17* following trauma also correlated with the activation kinetics of another established oxidative stress response regulator, *skn-1/NRF2* (Supplementary Fig. 6e, f).

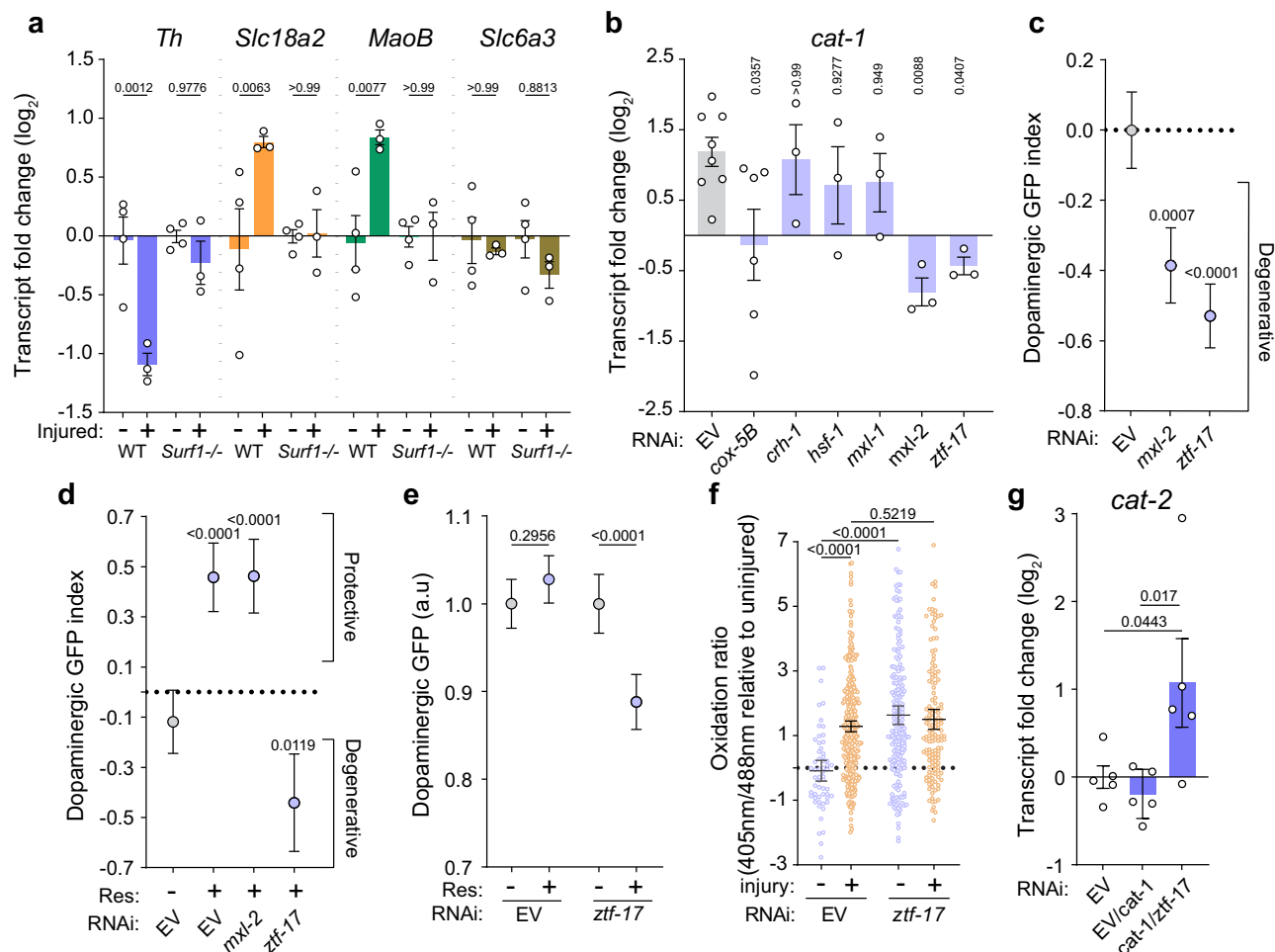


Fig. 3 | Identification of ZTF-17 as a critical regulator of the dopaminergic stress response in *C. elegans*. **a** Whole-brain RNA-seq from WT and *Surf1*^{-/-} mice 7 days post-TBI (GSE173431). Transcripts are normalized to time-matched uninjured controls. Ordinary one-way ANOVA with Šidák's correction. Mean ± SEM. *n* = 4 uninjured, *n* = 3 injured for WT and *surf1*^{-/-} mice. **b** qPCR quantification of *cat-1/Slc18a2* transcripts 48 h after injury on the respective RNAi conditions, normalized to uninjured controls. Ordinary one-way ANOVA with Dunnett's test. Mean ± SEM. *n* = 8 for EV, 6 for *cox-5B* positive control, and 3 for experimental RNAi. **c** Dopaminergic GFP retention in worms (PMD216) 48 h after injury. Positive and negative values show enhanced and reduced GFP retention respectively compared to injured EV control. ordinary one-way ANOVA with Dunnett's test. Mean ± 95%CI. From left to right, *n* = 1512, 1097, 1282 collected over 3 independent experiments. **d** Dopaminergic GFP retention in worms (PMD216) 48 h after injury treated with 30 μM reserpine or vehicle. Positive and negative values show enhanced and

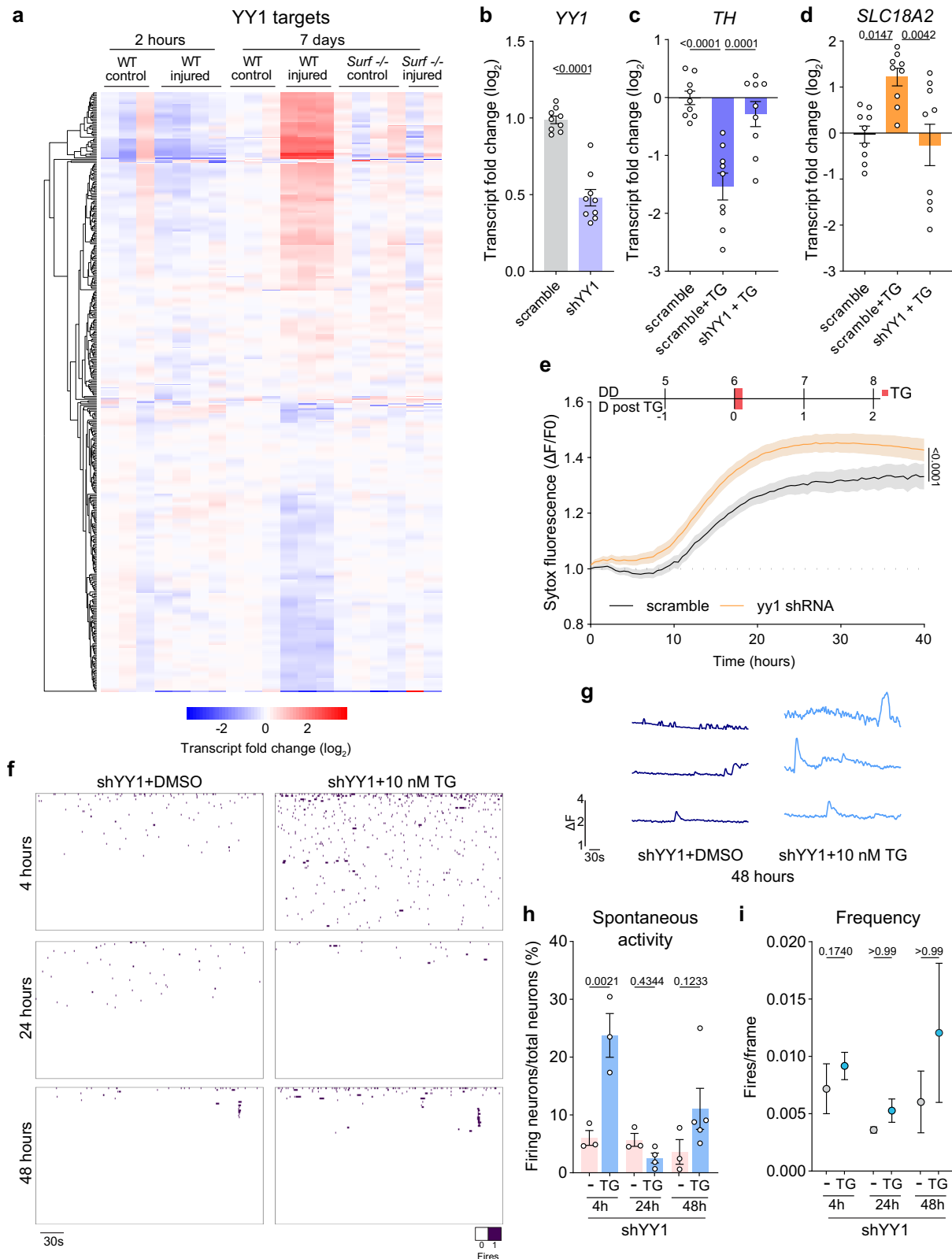
reduced GFP retention respectively compared to EV RNAi on vehicle control. Ordinary one-way ANOVA with Dunnett's test. Mean ± 95%CI. From left to right, *n* = 572, 885, 607, 874 collected over 3 independent experiments. **e** Dopaminergic GFP retention in day 3 adult worms (PMD216) raised on 30 μM reserpine or vehicle. Data is normalized to EV RNAi on vehicle control. Ordinary one-way ANOVA with Dunnett's test. Mean ± 95%CI. From left to right, *n* = 1082, 1147, 749, 1104 collected over 3 independent experiments. **f** Cytosolic ROS measurement in dopaminergic neurons using PMD249 raised on EV or *ztf-17* RNAi and injured at day 1 of adulthood. Data acquired 48 h post-injury. All samples normalized to the 405 nm/488 nm ratio of uninjured worms on EV. Ordinary one-way ANOVA with Šidák's correction. Mean ± 95%CI. From left to right, *n* = 58, 349, 205, 144. **g** qPCR quantification of *cat-2/TH* transcripts from day 1 adults (PMD216) raised on EV, mixed EV/*cat-1*, or *cat-1/ztf-17* RNAi. Ordinary one-way ANOVA with Šidák's correction. Mean ± SEM. *n* = 5 independent replicates.

YY1 mediates transmissive dormancy upon cellular stress

As the least divergent orthologue of *ztf-17* in mammals, YY1 is a ubiquitously expressed C2H2 zinc finger multidomain transcription factor implicated in embryonic development and cell lineage differentiation^{38,39}. YY1 is known to regulate a large set of genes associated with mitochondrial metabolism and aerobic glycolysis^{40,41}. Genome-wide transcriptomics revealed that the majority of YY1-regulated genes are differentially expressed after trauma in a time- and *Surf1*-dependent fashion, concurrent with DSR activation (Fig. 4a, Supplementary Fig. 7a). To determine whether YY1 is required for *TH* repression and *SLC18A2* activation, we established an IPTG-inducible shRNA system in the LUHMES cells to transiently knock down the expression of YY1 starting on day 2 of neuronal differentiation (Fig. 4b, Supplementary Fig. 7b, c). Consistent with our proposed model, decreasing YY1 expression by 55% via shRNA prevented the TG-

induced repression of *TH* and activation of *SLC18A2* as determined by qPCR (Fig. 4c, d). YY1 shRNA alone was also sufficient to increase *TH* baseline expression, suggesting that YY1 might regulate the expression of *TH* during unstressed conditions (Supplementary Fig. 7d). Baseline transcription of *SLC18A2* was, however, unchanged by YY1 shRNA (Supplementary Fig. 7e). With respect to stress-mediated protection, YY1 shRNA significantly worsened TG-induced cell death compared to scramble control as evidenced by SYTOX fluorescence (Fig. 4e), which is consistent with *ztf-17* RNAi enhancing trauma-induced dopaminergic degeneration in the worm (Fig. 3c).

Beyond regulating key components of dopamine metabolism, it was unclear whether YY1 also regulated neuronal function after TG treatment (Fig. 1b–e). To address this, we utilized the same calcium imaging regiment to understand how reduced YY1 expression would impact the frequency of spontaneous calcium transients in LUHMES



cells after treatment with TG. Remarkably, YY1 shRNA prevented the TG-mediated impairments (Fig. 4f–i, Supplementary Fig. 7f). Average amplitude was not impaired by TG treatments and, similar to naïve cells, TG modestly increased the amplitude at the later time points (Supplementary Fig. 7g). These observations introduce a potential role for YY1 as a regulator of stress-dependent silencing of neuronal activity.

Multimodal regulation of dopamine metabolism by YY1

Next, we wanted to elucidate the molecular mechanisms by which YY1 regulates *TH* and *SLC18A2* transcription under conditions of intracellular stress. Consistent with our proposed model that YY1 represses *TH* yet activates *SLC18A2*, YY1 functions both as a transcriptional activator and repressor^{42,43}. Along with its cofactor, CTCF⁴⁴, YY1 can also modulate gene expression by regulating 3-dimensional DNA looping and

Fig. 4 | YY1 is required for stress-induced regulation of dopamine metabolism and repression of neuronal activity in human dopaminergic neurons. **a** Relative transcript abundance of YY1 regulated genes (MSigDB TFT:TFT_legacy). Whole-brain RNA-seq from WT and *Surf1*^{-/-} mice 2 h or 7 days post-TBI. Samples normalized to uninjured, time-matched controls. Each lane per group corresponds to individual mice. **b** qPCR quantification of YY1 transcripts in LUHMES cells expressing scramble or YY1 shRNA. shRNA expression was induced for 5 days via IPTG. Unpaired two-tailed t-test. Mean \pm SEM. $n = 9$. **c, d** qPCR quantification of *TH* and *SLC18A2* transcripts in LUHMES cells expressing scramble control or YY1 shRNA treated with TG. Ordinary one-way ANOVA with Dunnett's test. Mean \pm SEM. $n = 9$ independent replicates. **e** SYTOX green fluorescence in LUHMES cells expressing scramble or YY1 shRNA after a 30 min TG pulse, ($\Delta F/F_0$). AUC was used for statistical analysis via an unpaired two-tailed t-test. DD = days of differentiation, D post TG = days after TG removal. Mean \pm SEM. $n = 10$ replicates. **f** Binary firing plots of

differentiated LUHMES cells with YY1 knockdown at corresponding timepoints post treatment. Plots show the 80 most active cells per condition as determined by frequency and are sorted accordingly from top to bottom. Total time of acquisition = 5 min (350 frames). Fluorescence time series were collected over 3 recordings/timepoint for DMSO treated cells and 3, 4, 6 recordings/timepoint for cells 4-, 24-, and 48 h post-TG, respectively. **g** Representative traces of the most active neurons per individual recording 48 h post-TG. Fluo-4 AM fluorescence is normalized to the intrinsic minimum fluorescence per neuron (ΔF). **h** Percentage of neurons with any spontaneous activity per recording. Ordinary one-way ANOVA with Sidák's correction. Mean \pm SEM. $n = 3$ recordings/timepoint for DMSO treated cells and 3, 4, 6 recordings/timepoint for cells 4-, 24-, and 48-hours post-TG, respectively. **i** Firing frequency of neurons with spontaneous activity. Recordings were collected at 1.16 FPS so 1 frame = 0.857 s. Ordinary one-way ANOVA with Sidák's correction. Mean \pm SEM. From left to right, $n = 37, 177, 39, 13, 18$, and 27.

chromatin architecture⁴⁵. To probe how YY1 regulates the expression of *TH* and *SLC18A2*, we analyzed publicly available YY1 and CTCF ChIP-seq datasets from human K562 cells. When comparing the *TH*, *SLC18A2*, and *YY1* loci, we observed distinct patterns of YY1 binding. In the case of *TH*, significant binding peaks for YY1 and CTCF were observed within the gene body at intron 10 with minimal promoter binding (Fig. 5a). While YY1 binding was enriched at the *SLC18A2* transcriptional start site, stronger binding peaks for both YY1 and CTCF were detected at an annotated distal enhancer element 25 kb upstream of the *SLC18A2* gene⁴⁶ (Fig. 5b). With respect to the *YY1* locus, there was significant binding of both YY1 and CTCF at and just past the transcriptional start site (Fig. 5c). Broadening our search to include 11 different cell lines with available YY1 ChIP-seq datasets, we observed similar binding trends. However, when assessing the binding of YY1 at intron 10 of *TH*, it became apparent that all of the cell lines displaying intronic binding were non-neural. In contrast, the neural-like cells NT2/D1 and SK-N-SH (with or without retinoic acid) had minimal binding of YY1 at *TH* intron 10 (Supplementary Fig. 8a), suggesting that this binding may be associated with cellular identity.

To determine the potential for stress-induced genomic binding by YY1 following aberrant calcium fluctuations, we employed YY1 CUT&RUN sequencing, also known as Cleavage Under Targets and Release Using Nuclease. Similar to the other neural cell lines, untreated LUHMES cells exhibited low YY1 binding at intron 10 of *TH*. Yet, we observed a >10-fold increase of YY1 binding at the first 250 bp of intron 10 24 h post-TG (Fig. 5d, g). For *SLC18A2*, a 2-fold TG-induced binding of YY1 was detected at its distal enhancer element rather than the *SLC18A2* transcriptional start site (Fig. 5e, g). We also observed increased YY1 binding at the transcriptional start site of *YY1*, underlining its transcriptional induction upon ionic and oxidative stress (Fig. 5f, g).

Intrigued by YY1's ability to undergo different mechanisms of stress-induced genomic regulation, we performed MACS2 peak calling of all YY1 enriched regions in control and stressed conditions. TG treatment initiated the formation of 351 new YY1 peaks compared to vehicle control (Fig. 5h, Supplementary Fig. 8b). Most of these stress-induced binding peaks appeared to follow a similar distribution with respect to genomic features, although there was a minor increase of promoter and intronic binding. At the same time, distal intergenic regions were decreased in the TG-induced YY1 peaks dataset compared to the control (Fig. 5i). However, there were noticeable differences in the types of genes bound by YY1 at the promoter versus gene body. Notably, GO-term analysis of promoter-bound genes showed an enrichment of genes involved in "response to ketones", "translational initiation", and "mRNA processing" (Supplementary Fig. 8c). Contrastingly, gene-body bound genes were enriched for "GTPase activity" and multiple categories involving presynaptic neuronal function (Supplementary Fig. 8d). We then cross-correlated genes with stress-inducible YY1 peaks and genes differentially regulated 7 days post-brain injury in mice. GO-term analysis of these gene sets identified that

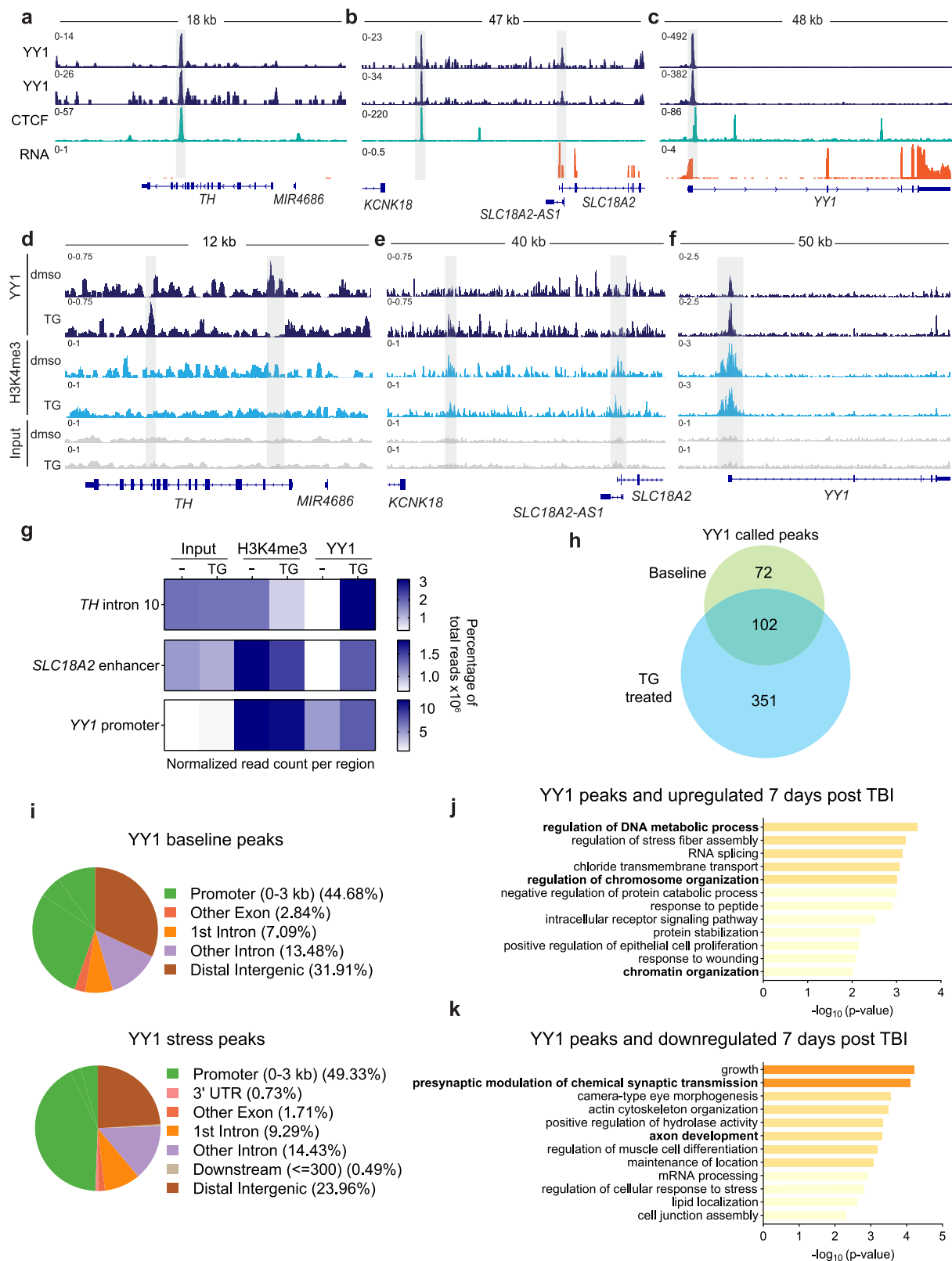
YY1 is associated with activating genes involved in DNA metabolic processes and chromosome organization while conversely repressing genes involved in cell growth, presynaptic chemical transmission, and axon development (Fig. 5j, k).

DNA damage and G4 formation facilitate YY1-mediated repression of *TH*

Next, we sought to obtain a molecular explanation for the distinct regulatory mechanisms employed by YY1 upon activation of the dopaminergic stress response. ChIP-seq and CUT&RUN datasets indicate binding of YY1 to intron 10 of *TH*, yet this region lacks consensus YY1 binding motifs (Supplementary Fig. 9a). As an alternate possibility, YY1 has recently been reported to bind guanine quadruplexes (G4s)^{47,48} which are secondary structures within DNA and RNA comprised of stacked guanine tetrads and have emerging roles in transcription, replication, genome instability, and DNA damage^{49,50}. Analysis of the *TH* gene body using distinct G4 prediction algorithms^{51,52}, identified a G4 within the same intron 10 region bound by YY1 (Fig. 6a). Small molecule G4 ligands can associate with these secondary structures and outcompete YY1 for G4 binding⁴⁷. To assess whether G4s form within intron 10 and are involved in YY1 recruitment, we analyzed YY1 ChIP-seq of HEK293 cells treated with the competitive G4 ligand TMPyP4. From this dataset, the magnitude of YY1 binding at intron 10 of *TH* was reduced (Supplementary Fig. 9b), providing evidence that G4s mediate this interaction between YY1 and intron 10 of *TH*.

Enrichment of G4 motifs occur in select genomic regions, including telomeres, promoters, transcription factor binding sites, as well as sites of double-stranded DNA breaks^{50,53}. Furthermore, G4s can be induced by guanine oxidation and subsequent APE1-mediated base-excision repair^{49,54}. Thus, trauma-induced oxidative stress could promote guanine oxidation, thereby driving G4 assembly at *TH* intron 10 and facilitating YY1 recruitment. To assess whether DNA damage occurred following the cellular stress induced by TG, we assayed the steady-state levels of the γ H2AX histone variant, whose levels correlate with the extent of DNA damage⁵⁵. We observed elevated γ H2AX levels as early as 6 h after TG treatment of LUHMES cells, as evidenced by western blot (Fig. 6b, c). In further support, genome-wide transcriptomics revealed the induction of several DNA-Damage Induced Transcripts (DDITs) 2, 3, and 4 at all time points tested after TG treatments (Supplementary Fig. 9c–e). Thus, DNA damage precedes the transcriptional repression of *TH* and could, therefore, reside upstream of YY1-dependent *TH* repression.

To further understand the possible involvement of DNA breaks in the DSR, we utilized ectopic means of inducing DNA damage. Application of the DNA damaging agent, etoposide, resulted in 3-fold repression of *TH* transcription, yet *SLC18A2* transcripts remained unchanged (Supplementary Fig. 9f, g), which is consistent with the presence of G4s within *TH* but not the *SLC18A2* enhancer. Yet it was unclear whether YY1 was sensing the damaged DNA itself or if it was downstream of the DNA damage response. Cellular responses to DNA



damage can act through the ataxia-telangiectasia mutated (ATM) or ataxia-telangiectasia and Rad3-related (ATR) kinase pathways⁵⁶. Since LUHMES cells are terminally differentiated in culture, we focused on the ATM kinase as ATR is more prominent in highly proliferative cells undergoing replicative stress⁵⁷. Inhibition of the ATM kinase prevents the DNA damage response and, thereby, the repair of endogenous DNA damage, allowing for the accumulation of basal double-stranded

DNA breaks. Therefore, if YY1 recruitment is directly driven by damaged DNA, *TH* repression would be induced. Alternatively, if YY1 were a downstream effector of the DNA damage response, *TH* repression would be abolished. In line with DNA damage directly inducing YY1 binding, the ATM inhibitor KU55933 was sufficient to repress *TH* transcription in LUHMES cells and even further potentiated TG-induced *TH* repression (Fig. 6d). Importantly, *TH* repression is still

Fig. 5 | YY1 regulates dopamine metabolism through distinct genomic element binding mechanisms. a–c Integrative Genomics Viewer (IGV) tracks of YY1 (ENCFF023AFF and ENCFF157ZKE) and CTCF (ENCFF050CCI) ChIP-seq combined with RNA-seq (ENCFF130RGZ) in K562 cells. Tracks display fold change over control of pooled replicates for ChIP-seq and signal of unique reads for RNA-seq. Regions of interest are highlighted by the shaded area. **d–f** Integrative Genomics Viewer (IGV) tracks displaying YY1 and H3K4me3 CUT&RUN 24 h after a 30-minute pulse with TG at a final concentration of 10 nM in terminally differentiated LUHMES cells. Tracks display counts per million normalized aggregate reads from pooled replicates. $n = 6$ per condition. Regions of interest are highlighted by the shaded area. **g** Quantification of read counts per region normalized to the total read counts per

sample multiplied by 10^6 . Regions used for the analysis were the following: *TH* intron 10 (chr11:2,166,250–2,166,500), *SLC18A2* enhancer (chr10:117,216,450–117,217,450), *YY1* promoter (chr14:100,239,250–100,240,000). Counts per region were scaled to 1 kb prior to total read count normalization. **h** MACS2 called YY1 peaks in control and TG stressed groups. Minimum FDR (q -value) cutoff for peak detection was set at 0.05. Peaks were considered overlapping when called peak-BEDs had ≥ 1 overlapping bp. **i** Annotation of genomic elements overlapping with YY1 peaks via ChIPseeker analysis of YY1 called peaks in control (upper) and TG treated (lower) terminally differentiated LUHMES cells. **j, k** GO-term gene set enrichment analysis of genes with YY1 peaks and differential expression (multiple t -test, $p < 0.05$) 7 days after traumatic brain injury.

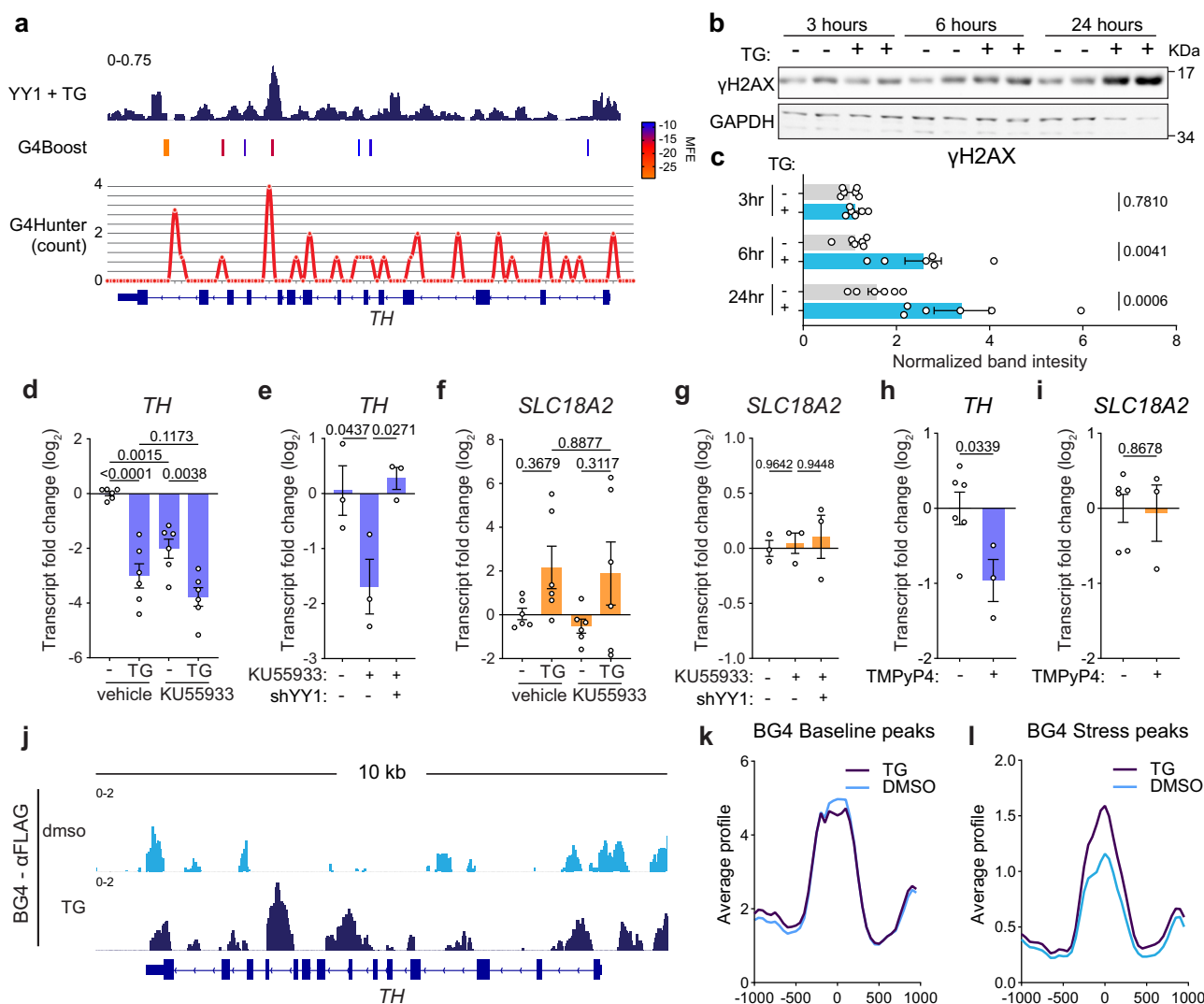


Fig. 6 | DNA damage and stress-dependent guanine quadruplex formation facilitate YY1-mediated repression of *TH*. **a** Computational prediction of guanine quadruplexes (G4) along the *TH* gene body according to G4Boost³¹ and G4Hunter³². Top track indicates YY1 CUT&RUN reads of terminally differentiated LUHMES cells 24 h post-TG treatment (same data as Fig. 6d). Middle track displays G4Boost prediction of folded G4s and is color-coded according to the predicted minimum free energy (MFE). Bottom track signal indicates the number of potential guanine quadruplexes within *TH* as predicted by G4Hunter. The sequence displayed highlights the region where YY1 binding overlaps with the predicted G4 structures. **b** γH2AX levels determined by western blot of LUHMES cells 3, 6, and 24 h after TG treatment. Blotted for phosphorylated γH2AX and GAPDH. **c** Quantification of γH2AX normalized to GAPDH and 3 h untreated control. Ordinary one-way ANOVA with Šidák's

correction. Mean \pm SEM. $n = 6$ independent replicates. **d, f** qPCR quantification of *TH* and *SLC18A2* transcripts in LUHMES cells after TG and/or 10 μ M KU55933 treatment. Ordinary one-way ANOVA with Dunnett's test. Mean \pm SEM. $n = 6$ independent replicates. **e, g** qPCR quantification of *TH* and *SLC18A2* transcripts in LUHMES cells expressing scramble control or YY1 shRNA treated with 10 μ M KU55933 for 24 h. Ordinary one-way ANOVA with Dunnett's test. Mean \pm SEM. $n = 3$ independent replicates. **h, i** qPCR quantification of *TH* and *SLC18A2* transcripts in LUHMES cells after a 24 h treatment with 5 μ M TMPyP4. Unpaired two-tailed t -test. Mean \pm SEM. $n = 6$ independent replicates for vehicle control and $n = 3$ for TMPyP4 treated cells. **j** IGV browser tracks of BG4 CUT&RUN signal normalized to αFLAG control collected 24 h post-TG challenge. **k, l** Average profiles of BG4 signal at regions retrieved from MACS2 peak calling of vehicle or TG treated cells, respectively.

dependent on YY1 since co-administering YY1 shRNA abolished the ability of KU55933 to repress *TH* (Fig. 6e). Consistent with the differential effect of etoposide on *TH* and *SLC18A2*, KU55933 treatment had no effect on *SLC18A2* transcription or its induction by TG (Fig. 6f, g). Thus, DNA damage is sufficient to induce *TH* repression, seemingly independent of the ATM-mediated DNA damage response.

With regards to YY1 and G4 interactions repressing *TH*, we reasoned that DNA damage-induced G4 formation and subsequent YY1 binding could stabilize these transient structures similarly to G4 stabilizing ligands⁴⁷. This stabilization could in turn, lead to transcriptional repression via direct impairment of RNA polymerase II transcription⁵⁸. To test this, differentiated LUHMES cells were treated with the G4 stabilizer TMPyP₄, which, despite decreasing YY1 occupancy at *TH* intron 10 (Supplementary Fig. 9b), was sufficient to repress *TH* transcription without affecting *SLC18A2* levels (Fig. 6h, i).

To understand how cellular stress alters the G4 genomic landscape in LUHMES cells, G4 CUT&RUN was performed 24 h post-TG challenge using the FLAG-tagged BG4 single-chain fragment variable (scFv) and an α -FLAG secondary antibody. BG4 coverage normalized to α -FLAG control conditions revealed a substantial enrichment at *TH* intron 10 in TG-treated cells but not in unstressed controls (Fig. 6j). We further confirmed this via CUT&RUN qPCR with primers targeting the sequence flanking the predicted G4 (Supplementary Fig. 10a). Intriguingly, existing G4s present at baseline were minimally affected upon TG treatment. In contrast, stress-inducible G4s emerging in TG-treated cells had substantially increased BG4 signal compared to vehicle controls (Fig. 6k, l and Supplementary Fig. 10b–d). This supports the notion of distinguishable steady-state and stress-inducible G4 populations. As an example, the *SLC20A1* promoter had significantly enriched BG4 signal over control only upon TG treatment, and this corresponded to TG-induced YY1 binding (Supplementary Fig. 11a). Gene set enrichment analysis of all genes with stress-induced BG4 peaks revealed an enrichment of genes related to neuronal and synaptic function, potentially linking this stress-inducible subset of G4s with the neuronal dormancy phenotype described earlier (Supplementary Fig. 11b, c). These data suggest a model in which DNA damage promotes transient G4 formation at genes involved in neuronal function, including *TH* intron 10. This subsequently recruits YY1, which in turn stabilizes these transient G4 assemblies and allows for stress-dependent transcriptional regulation. Yet the degree to which this YY1 dependent stress response is dictated by G4 formation and what targets might be regulated independently and in parallel, such as *SLC18A2*, remain outstanding questions.

G4 stabilization in *TH* intron 10 inhibits polymerase transcription

To identify the minimal sequence within *TH* intron 10 capable of folding into a G4 confirmation, circular dichroism (CD) was performed on 6 overlapping ssDNA fragments of 40 bp tiling intron 10 (Fig. 7a). This revealed a strong parallel G4 fold in fragment 3 and 4, which share a core of 3 out of 4 required guanine stretches (Supplementary Fig. 12a–c). The strongest G4 signature was observed in fragment 4, which was even more pronounced than the previously reported parallel G4 in the MYC promoter⁵⁹ (Fig. 7b). Furthermore, addition of G4 stabilizer TMPyP₄ or recombinant YY1 protein did not alter its parallel G4 confirmation, in line with a previously reported parallel G4 structure⁴⁷ (Supplementary Fig. 12d). In further support, the melting temperature of the ssDNA was significantly higher in the presence of TMPyP₄ compared to vehicle control (Fig. 7c and Supplementary Fig. 12e).

G4s within the gene body have been implicated in reduced transcription through varying mechanisms of RNA Polymerase II stalling^{60–62} and we sought to determine whether G4 stabilization in intron 10 could inhibit polymerase readthrough. To this end, we constructed *TH* expression plasmids using its cDNA and engineered intron

10 (*TH*+10) at its endogenous location. As a control, we generated a similar construct with *TH* intron 6 (*TH*+6) inserted in its endogenous location, which has a similar GC content and is of comparable length as intron 10 (Fig. 7d). Using primers flanking either intron, amplification efficiency was assessed in the presence of varying TMPyP₄ concentrations via semi-quantitative PCR. While amplification of *TH* cDNA and *TH*+6 occurred using a standard Taq polymerase, the *TH*+10 construct yielded no observable PCR product under any condition (Supplementary Fig. 13a). Conversely, primers targeting the plasmid backbone amplified without impairment for all constructs. The addition of TMPyP₄ also did not affect *TH* cDNA and *TH*+6 amplification, nor did it impair backbone amplification (Supplementary Fig. 13a). These observations suggest that *TH* intron 10 sterically hinders the progression of the Taq polymerase. The same experiments were repeated using a high-fidelity polymerase which enabled the amplification of the *TH* intron 10 region (Fig. 7e). However, *TH*+10 amplification was reduced in a TMPyP₄ dose-dependent manner when compared to *TH* cDNA and *TH*+6, which both remained refractory to this G4 stabilization (Fig. 7e, f).

While these data support that G4 stabilization within intron 10 directly inhibits polymerase readthrough, it's unclear whether this would also occur within the cell. Thus, we engineered *TH* expression plasmids, which enabled us to monitor *TH* transcription and translation by measuring the fluorescence intensity of the mCherry fluorophore residing at the C-terminus of the *TH* gene product. Under control of the constitutive CMV promoter, *TH*+6-mCherry and *TH*+10-mCherry were ectopically expressed in HEK293t cells supplemented with varying concentrations of TMPyP₄ (Fig. 7g) (Supplementary Fig. 13b). After the initial transfections, quantification of mCherry fluorescence revealed that *TH*+10 production was inhibited by TMPyP₄ and had a more sensitive dose-response compared to *TH*+6 (Fig. 7h and Supplementary Fig. 13c). Intriguingly, the highest TMPyP₄ concentration abolished mCherry fluorescence for both *TH* expression plasmids, which could be due to forced stabilization of imperfect G4's in the cDNA or perhaps RNA transcripts. Taken together, our data suggests that intron 10 alone is sufficient to repress *TH* expression via G4 stabilization.

Discussion

Cellular stress can rapidly activate a number of cytoprotective pathways. Yet, we sought to overwhelm these established pathways and determine whether the small subset of resilient neurons deployed alternate, last-resort protective measures. Herein, we propose that dopaminergic neurons harbor a unique adaptive mechanism that enables them to prioritize their viability over their transmissive function under times of severe cellular stress. While impairment of dopaminergic function by various stressors has been broadly reported, the underlying molecular mechanism has remained enigmatic. We propose the existence of a dopaminergic stress response (DSR) as a potential molecular explanation for this phenomenon. Yet many outstanding questions remain: how and if these dormant dopaminergic neurons might reinitiate their full signaling capacity, and whether prolonged periods of dormancy can have deleterious effects on their long-term viability and function. Although protective against acute challenges, how long should an active halt of neurotransmission persist? Assuming reactivation is possible, is there a time window for neurons to regain healthy and robust functionality after a period of dormancy? Lastly, do other neuronal subtypes or cells throughout the body initiate a similar state of dormancy or inactivity to favor survival over function under times of stress?

While most adaptive strategies to counteract cellular stress are ubiquitous and observable in several cell types, this stress response is highly cell-type specific due to some of the enzymes and regulators modulated by YY1. Moreover, this highlights how an individualized stress response can be specifically tuned to accommodate the inherent

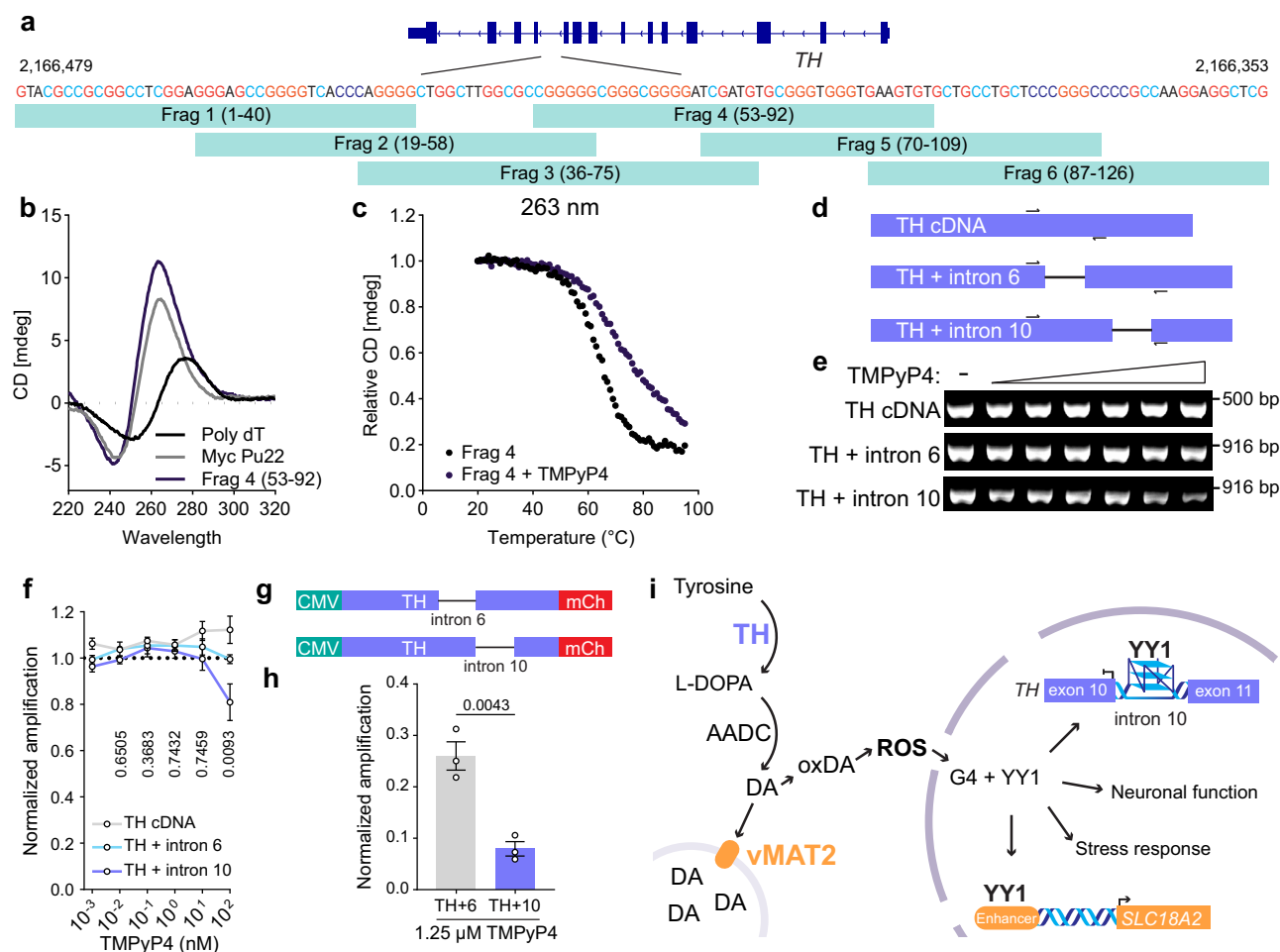


Fig. 7 | *TH* intron 10 folds into a parallel G4 with the potential to directly inhibit polymerase transcription. **a** Coding strand sequence of the first 126 bp of *TH* intron 10 which surrounds the predicted G4. Grey blocks illustrate sequences of probes tested for G4 folding using CD. **b** CD spectra of fragment 4 (Frag 4 53-92), positive parallel G4 control Myc Pu22, and a poly dT negative control. Spectra are an average of 10 accumulations **(c)** relative ellipticity of fragment 4 with or without TMPyP₄ at 263 nm and a temperature range of 20–95 °C. **d** DNA construct and primer design used for in vitro G4 polymerase inhibition assay. **e** PCR products amplified by the high fidelity Q5 polymerase. Final TMPyP₄ concentration from left to right was 0, 0.1 nM, 1 nM, 10 nM, 100 nM, 1 μM, 10 μM. **f** Quantification of product

shown in **(e)**. Band intensity was normalized to internal, vehicle control. Statistical analysis was performed using a two-way ANOVA with mixed-effects analysis and Dunnett's test. *p* values represent *TH* + intron 10 at the respective TMPyP₄ concentration compared back to 10–3 nM TMPyP₄. Mean ± SEM. *n* = 4 independent replicates per condition. **g** DNA construct design used for in vivo G4 inhibition assay. **h** mCherry amplification 60 h post-transfection and treated with 1.25 μM TMPyP₄. Data is normalized to time-matched, untreated controls. Mean ± SEM. Statistical analysis was performed using an unpaired two-tailed t-test. For statistical analysis of the entire dose response curve see Supplementary Fig. 13c and source data. *n* = 3 independent replicates per condition. **i** Proposed model of DSR regulation.

molecular composition of the cell. While our study focused on functional impairment of dopaminergic neurons, other specialized stress responses might extend to other neuronal subtypes or beyond the nervous system. The proposed regulation of dopamine homeostasis appears distinct from conventional autoreceptor feedback mechanisms, which function to ensure neurotransmission by sensing dopamine released into the synaptic cleft rather than responding to changes in intracellular dopamine. When dopamine is released into the synapse, D2-type autoreceptors inhibit the adenylate cyclase leading to PKA and CREB activity which are broad positive regulators of dopamine synthesis and release³⁰. Rather, our data suggests that the DSR is able to override autoreceptor feedback and repress dopamine synthesis when dopamine is elevated in the cytosol despite its depletion in the synaptic cleft. While this is beneficial for cellular survival, repressing dopamine synthesis likely has severe consequences on the functionality of these dopaminergic neurons and their integrated neural circuitry. Future studies should investigate whether this regulation of dopamine metabolism extends beyond the stress response described in this study, as it might also play a role in minimizing cytosolic dopamine in healthy neurons.

Based on the implication of DNA damage, the correlation between stress-induced YY1 binding and predicted G4s, and the sufficiency of G4 stabilization to repress *TH*, we propose a mechanism where oxidative damage to DNA allows for the formation of transient G4 structures, which are bound and further stabilized by YY1 (Fig. 7i). This can subsequently drive transcriptional repression by blocking RNA polymerase II from faithfully transcribing *TH*. Intriguingly, activation of dopamine packaging and likely other stress-responsive YY1 targets appeared independent of this mechanism, illustrating the diverse mechanisms of regulation utilized by YY1 to orchestrate the DSR. While we observed YY1 peaks at the intron 10 region of *TH* in various non-neuronal cells during unstressed conditions, it remains unclear if this YY1 binding functions through a similar mechanism. Since the *TH* gene is presumably not actively transcribed in these cell lines, it is therefore possible that other epigenetic mechanisms are regulating G4 folding depending on the state of chromatin accessibility. While G4 stabilization is sufficient to repress *TH*, we cannot fully rule out the contribution of additional forms of transcriptional regulation employed by YY1, such as co-factor interactions, recruitment of epigenetic regulators, or regulation of the higher-ordered DNA architecture. Furthermore, while our data implies that

YY1-mediated *TH* repression occurs through oxidation-induced DNA damage and G4 stabilization, it remains unclear how YY1 facilitates the activation of several other catecholamine-related genes, such as *SLC18A2*. Given the rapid response of *SLC18A2* activation to stress, post-translational modifications of YY1 emerge as likely candidates. Indeed, YY1 has been demonstrated to be a substrate for O-GlcNAcylation⁶³, methylation⁶⁴, ubiquitination⁶⁵, acetylation⁶⁶, poly(ADP-ribosyl)ation^{67–69}, SUMOylation⁷⁰, S-nitrosation⁷¹, and phosphorylation⁷² by various enzymes, with several of these modifications implicated in response to diverse cellular stressors, including metabolic or genotoxic perturbations^{69,73}. Beyond post-translational modifications, YY1 has been identified as a substrate for caspase cleavage⁷⁴, offering an additional avenue for stress-induced regulation of YY1 activity. Unraveling the mechanisms governing YY1 activity in the context of the DSR should be a key focus of future studies. Notably, our YY1 CUT&RUN results indicate that transcriptional changes primarily result from increased YY1 binding rather than a loss of YY1 occupancy. Additionally, investigating the potential crosstalk between different stress response pathways, such as the integrated stress response and their impact on YY1 activity, could provide further insights into the intricacies of neuronal adaptation to stress.

While this study focused on the regulation of dopamine homeostasis by YY1, YY1 likely regulates other genes related to neuronal function in a stress-dependent manner. Peak calling analysis of YY1 upon TG revealed multiple candidate genes that could be responsible for stress-induced dormancy. These include multiple ion channels such as a potassium voltage-gated channel (*KCNB2*), a potassium sodium-activated channel (*KCNT2*), a glutamate receptor (*GRID2*), a calcium-gated channel (*CACNA1E*), and Protein kinase C gamma (*PRKCG*) which has been linked to synaptic plasticity and long-term potentiation/depression. Further investigation is required to test whether any of these genes are required for YY1-dependent dormancy. It is worth noting that we assessed neuronal activity through the proxy of calcium transients. While intracellular calcium fluctuations are a reliable correlate of depolarization⁷⁵, it does not always reflect the electrophysiological state of the neuron. Future studies should investigate whether YY1 also modulates the more intricate electrophysiological changes in dopaminergic neurons reported to occur upon cellular stress^{13,15,17}.

Mechanistically, the role of G4s linking cellular stress and DNA damage to transcriptional regulation by YY1 could have far-reaching implications. In this manuscript, we focused on its role in regulating *TH* transcription, yet genome-wide analysis does suggest increased G4 formation upon cellular stress. Beyond this, YY1 is not the only G4-binding protein. It would, therefore, be of great interest to characterize what stress-inducible G4s modify stress resilience and through what factors this might occur.

Lastly, understanding the broader network of molecular events surrounding YY1 in the context of dopaminergic neurons could lead to new therapeutic strategies for Parkinson's Disease and possibly other neurological disorders. Notable means of treating Parkinson's Disease include drug therapies designed to enhance dopamine levels in an effort to reactivate dormant circuits, including L-DOPA, dopamine agonists, and MAO inhibitors. In more extreme cases, deep brain stimulation has successfully been used to rouse these dormant circuits from their slumber. While it remains to be seen whether YY1 has the capacity to induce transmissive dormancy in a clinical setting, there is strong potential for YY1 to be a druggable target to modulate either dopaminergic survival or function.

Methods

Cell culture

Lund's Human Mesencephalic Embryonic Stem cells (LUHMES; ABM T0284) were maintained as embryonic precursors in T75 flasks coated with poly-L-Ornithine (Sigma Aldridge P4957) and fibronectin

(Millipore Sigma FC010) using complete growth media consisting of advanced DMEM/F12 (Fisher Scientific 12-634-010) N2 supplement (Fisher Scientific 17-502-048), Glutamax (Fisher Scientific 35-050-061), penicillin/streptomycin (Sigma Aldridge P4333), and recombinant human FGF (ABM Z101456). Prior to all experiments, LUHMES were differentiated into mature human dopaminergic neurons by replacing the complete growth media with differentiation media containing advanced DMEM/F12, N2 supplement, Glutamax, penicillin/streptomycin, dbcAMP (Santa Cruz Biotechnology sc-201567B), tetracycline (RPI T17000), and recombinant human GDNF (ABM Z101055). On day 2 of differentiation, LUHMES were trypsinized and seeded at a density of 1.8×10^5 cells/cm² in coated 6- or 24-well plate. Differentiation media was replaced every 2 days. On day 6 of differentiation, LUHMES were considered mature, differentiated dopaminergic neurons and were treated with experimental conditions.

hTERT immortalized normal human astrocytes (NHA; ABM T0281) were cultured according to manufacturer's recommendations in Prigrow IV medium (ABM TM004), supplemented with 10% FBS (Sigma Aldridge F0926), 10 ng/ml EGF (ABM Z100139), Glutamax (Fisher Scientific 35-050-061), and 1% penicillin/streptomycin (Sigma Aldridge P4333). NHA cells were always grown on plates coated with Applied Cell Extracellular Matrix (ABM G422).

Cytosolic calcium stress was induced by treating day 6 terminally differentiated LUHMES cells with thapsigargin (TG; Fisher Scientific AC328570010), a non-competitive inhibitor of the sarco/endoplasmic reticulum Ca²⁺ ATPase (SERCA), dissolved in DMSO and diluted 1000x in differentiation media to reach the final concentration of 10 nM. After 30 min of TG treatment, media was aspirated, and fresh differentiation media was added. Control cells were treated with DMSO vehicle equally diluted in media. Cell death was measured by adding SYTOX green (Thermo Fisher Scientific S7020) at a final concentration of 200 nM and fluorescence was monitored using a CLARIOstar temperature and atmosphere controlled fluorescent plate reader (BMG Labtech). Significance between traces was determined by calculating the 95% confidence interval of the total area under the curve. Reserpine (Sigma-Aldrich 83580) pre-treatment was started at day 5 of differentiation while reserpine post-TG treatment was added after the TG containing media was replaced and reserpine was present during the remainder of the experiment.

pLV[shRNA]-LacI:T2A:Puro-U6/2xLacO>Scramble_shRNA and pLV[shRNA]-LacI:T2A:Puro-U6/2xLacO>hYY1[shRNA#3] lentiviral constructs were obtained from VectorBuilder Inc. (Chicago, IL) and transfected into HEK293T cells using jetPRIME (VWR 89129). Virus containing media was collected every 24 h for 4 consecutive days. Media was centrifuged at 400 xg for 5 min and supernatant was filtered through a 0.45 µm filter (Fisher Scientific 09-720-005) to remove any HEK293T cells. Undifferentiated LUHMES cells were cultured in a 6-well plate with LUHMES growth media + 4 µg/ml polybrene and infected with 200 µL of viral supernatant. Media was replaced 24 h after infection and cells were allowed to recover for an additional 24 h until puromycin selection was initiated. Puromycin resistant cells were then amplified in bulk, treated with puromycin again to confirm resistance, and IPTG inducible shRNA mediated knock down was confirmed via western blot and qPCR.

The following drugs were used in cell culture experiments and were always dissolved in the appropriate media from a 1000X stock solution; reserpine (Sigma-Aldrich 83580) dissolved in acetic acid, paraquat (Fisher Scientific AC227320010) dissolved in water, etoposide (Fisher Scientific 50-719-1) dissolved in DMSO, KU55933 (Selleck Chemicals S1092) dissolved in DMSO, TMPyP4 (Sigma-Aldrich 323497) dissolved in water.

Live-cell calcium imaging

Calcium imaging was performed using a Leica DMI8-CS confocal microscope equipped with one photomultiplier tube, two super-

sensitive hybrid HyD detectors, and highly stable lasers (UV/405 nm DMOD compact, 488 nm, 552 nm, 638 nm). Videos were acquired through a HC PL APO CS2 20x/0.75 IMM objective. To enable oil objective imaging, cells were differentiated on glass-bottom culture plates (#1.5 cover glass 0.170 ± 0.005 mm) (Cellvis P06-1.5H-N). 1 h prior to imaging, cultured neurons were loaded with 4 μ M Fluo-4 AM (Fisher Scientific F14201) for 30 min at 37 °C in the dark. Cells were subsequently washed once with artificial cerebral spinal fluid (ACSF) (125 mM NaCl, 5 mM KCl, 2 mM CaCl₂, 1 mM MgCl₂, 10 mM HEPES, 25 mM D-Glucose, dissolved in deionized water, and pH adjusted to 7.4). After one wash, neurons were maintained in ACSF for the remainder of the experiment. Prior to recording, cells were placed at room temperature for 20 min in the dark to allow for complete deesterification of the Fluo-4 dye. Cells were subsequently placed in a temperature and CO₂ controlled chamber (Okol UNO stage 158006104) including objective heater. The objective, chamber, and immersion oil (type G, Leica 11513910) were all preheated to minimize focal drift induced by temperature equilibration of the immersion oil during acquisition. Images were acquired using the 488 nm laser set at 0.1% laser power and fluorescence was detected using HyD detectors set at 50% gain. 5 min recordings were collected per sample at a frame rate of 1.16 fps (350 frames/5 min).

Fluorescent quantification was performed using ImageJ. First, timeseries were stabilized for x-y drift using the “Linear Stack Alignment with SIFT” plugin. Using the ImageJ ROI manager, regions were manually drawn within all visible soma in view. Raw fluorescent data was subsequently exported and analyzed using MATLAB (R2023b). First, each value was normalized to the row average to account for drift of photobleaching of total fluorescent signal across all cells. Values were then normalized to each column's (neurons) minimum value obtained over the entire series. Firing events were subsequently identified as any value that increased > 1.1 fold in normalized fluorescence over the average of the 5 frames prior. The start of each fire was used to calculate firing frequency and the maximum peak fluorescence per fire was used for mean amplitude calculations. Any neuron with at least 1 fire per series was considered to possess spontaneous activity. Heatmaps were generated based on the binary firing matrix described above.

Western blotting

1–2 million cells were collected per condition in RIPA buffer supplemented with 1X EDTA-free protease inhibitor cocktail (Roche 11836170001), and 1× phosSTOP phosphatase inhibitor cocktail (Roche PHOSS-RO). Lysates were incubated on ice for 30 min and vortexed every 10 min, passed through a 29 ½ gauge insulin syringe, and cleared by centrifugation for 15 min at 20,000 × g and 4 °C. Protein concentration was determined by BCA protein quantification kit (Thermo Scientific 23225) and samples were adjusted to an equivalent concentration using RIPA lysis buffer. Lysates were then supplemented 3:1 with Laemmli 4× SDS sample buffer (Bio-Rad 1610747) + BME (Sigma Aldridge M3148) and boiled at 90 °C for 10 min. Samples were then resolved by 10% bis/acrylamide SDS-PAGE electrophoresis, transferred to nitrocellulose membranes using Bio-Rad Trans-Blot turbo, and subjected to analysis by western blot. All antibodies were diluted in 5% BSA/TBS. Rabbit anti-TH (Cell Signaling Technology 2792) and rabbit anti-YY1 (Cell Signaling Technology 46395S) were diluted 1:1,000 and mouse anti-GAPDH (Sigma G8795) was diluted 1:2,500. All secondary antibodies, IRDye® 680RD Goat anti-Mouse IgG (LI-COR 926-68070) and IRDye® 800CW Goat anti-Rabbit IgG (LI-COR 926-32211) were diluted 1:5,000. Blots were imaged using a ChemiDoc (Bio-Rad) at the highest resolution and exposure was done automatically. Band intensities were quantified using Image Lab (Bio-Rad version 6.1).

Molecular cloning

All cloning was done using Gibson assembly (NEB E2611L) following the standard NEB recommended procedures. Briefly, all inserts were

amplified with addition of a 15 to 20 nucleotide overhang with homology to the recombination targets. All cloning PCR reactions were performed using the Q5 high fidelity polymerase (NEB M0491S). Clean amplification products were confirmed via agarose gel electrophoresis and 50–150 μ l PCR reactions were combined and purified using the Monarch® PCR & DNA Cleanup Kit (NEB T1030S). Insert and vector were mixed at the recommended 3-fold molar excess of the insert with 50–100 ng of PCR linearized vector backbone. Gibson assembly master mix (2x) was then added to the mixture and incubated at 50 °C for 15 min and subsequently transformed into NEB 5-alpha competent *E. coli* cells.

TH intron constructs were made by insertion of genomic introns into full length cDNA of human tyrosine hydroxylase, transcript variant 2 (NM_000360.3) (Sino Biological). GFPspark was replaced with mCherry. All cloning primers used are listed in Supplementary Table S1.

RNA extraction

RNA was extracted from 1500 to 2000 worms per condition using phenol-chloroform extraction. Briefly, 1 ml of Trizol was added to 100 μ l of age synchronized worm pellets and then flash-frozen in liquid nitrogen. Worms were then lysed by repeated freeze-thaw cycles and 200 μ l of chloroform was added and incubated for 3 min at RT. The aqueous phase was separated by spinning at 12,000 × g for 10 min at 4 °C and transferred to a new tube for isopropanol/ethanol precipitation of RNA. LUHMES RNA was extracted using the Invitrogen PureLink RNA kit (Invitrogen 12183018 A) using manufacturers provided protocol.

Quantitative PCR

1 μ g of extracted RNA was reverse transcribed using a QuantiTect Reverse Transcription kit (Qiagen 205311) following the manufacturer's protocol, which includes a genomic DNA elimination step. qPCR was performed with the iTaq Universal SYBR Green Supermix kit (Bio-Rad 1525125) and the CFX384 Real-Time System (Bio-Rad). Each well contained 50 ng of cDNA and primers at a concentration of 300 nM each. Samples were loaded in technical triplicate with biological replicates of three or more. Primer pair selectivity was confirmed by melting curve analysis, and wells with more than one melt peak were excluded from the analysis. Relative transcript abundance was calculated by normalizing to housekeeping genes *tba-1* and *Y45F10D.4* for *C. elegans* samples and *GAPDH* for human samples using the $\Delta\Delta C_t$ method. All primers used are listed in Table S1.

Dopamine ELISA

The cellular dopamine concentration was determined using a competitive dopamine ELISA (Novus Biologicals) following manufacturers recommended procedure. Briefly, cells were washed with PBS and subsequently scraped and transferred to a 1.5 ml tube. Cell pellets were washed three more times with PBS and then lysed via freeze-thaw repetition in liquid nitrogen. Remaining cell fragments were then removed with a 10 min spin at 1500 × g and supernatants were used to carry out the ELISA. Absolute quantification of dopamine was calculated via a standard curve and normalized to total protein present in the lysed sample.

RNA-sequencing

Quality control, mRNA purification, and paired-end 150 bp Illumina sequencing were performed by Novogene (Sacramento, CA). mRNA was enriched using oligo(dT) beads, randomly fragmented in fragmentation buffer, and reverse transcribed to cDNA using random hexamers. Following first-strand synthesis, Illumina synthesis buffer was added with dNTPs, RNase (H) and *E. coli* polymerase I to synthesize the second strand by nick-translation. The cDNA library was purified, underwent terminal repair, A-tailing, and ligation of adapters before

PCR enrichment. The cDNA library concentration was quantified with a Qubit 2.0 fluorometer (ThermoFisher Scientific) and sized with an Agilent 2100 Bioanalyzer (Agilent). RNA-seq statistical analysis was performed using CLC software (version 9.0, CLC Bio, Aarhus, Denmark). Data is presented as reads per kilobase million (RPKM) with values normalized to control levels made relative to 0.

Gene Set Enrichment Analysis (GSEA)

GSEA was performed on differentially expressed genes with a *P*-value < 0.05 compared to control. GO-term biological process or KEGG annotation was performed on gene sets using metascape.org to identify overrepresented pathways undergoing transcriptional changes. Pathways with significant overlap in gene set were ranked based on FDR *q*-value and the 20 most significantly changed pathways were presented.

Bioinformatic screening of transcription factor candidates

TFT:TFT legacy analysis was performed to identify transcription factors with differential expression of downstream targets using gsea-msigdb.org and the top 50 hits were used for further analysis. Other filtering constraints included that transcription factors must have annotated homologues in both mice and worm, must be annotated to be expressed in dopaminergic neurons according to CeNGEN, and have predicted binding sites in the promoter region (4 kb upstream of transcription start site) of the *SLC18A2* according to tfbind.hgc.jp.

Closed head traumatic brain injury

Adult mice of at least 8 weeks of age were used in this study. *Surf1* +/+ and *Surf1*−/− (RRID:MGI:3698949) were obtained from Massimo Zeviani (University of Cambridge). The closed head traumatic brain injury was induced using our upright, railed-guided weight drop device developed and validated previously³⁴. Briefly, a weight of 220 g was dropped on a brass impactor with a nylon tip. Prior to injury, mice were anesthetized with vaporized isoflurane/oxygen in a chamber connected to an inhalation anesthesia system (Cat. No. 901810; VetEquip). Vaporizer settings were set to 3% USP grade isoflurane and 2.5 lpm USP grade oxygen. Anesthetized mice were placed on a memory foam cushion resting on a height-adjustable platform. The desired site of impact was localized on the head of mice and the impactor tip was placed directly in contact with that site. Once positioned, the weight was released by activating an electronic trigger, hitting the impactor. Immediately following injury, mice were placed on their backs to record the righting reflex recovery time confirming a successful impact. After recovery, mice were placed back in their cage with food and water *ad libitum*. Control mice received only anesthesia and were not subjected to impact, but their righting reflex recovery time was also recorded in the same manner as for the injured mice. All closed head traumatic brain injury experiments were subject to approval by the Institutional Animal Care and Use Committee (IACUC) (Protocol No. 2016–101750) and performed in accordance with institutional and federal guidelines.

C. elegans strains and maintenance

All strains were maintained on standard NGM plates seeded with OP50 bacterial lawn and were kept in a dark 15 °C incubator. For experiments requiring large numbers of worms, stock plates were chunked onto OP50 seeded HGM plates and incubated at 20 °C and age-synchronization was performed by hypochlorite treatment of gravid animals.

The following strains were obtained from the CGC: N2, CF512 (*rrf-3(b26) II; fem-1(hc17) IV*), WM27 (*rde-1(ne219) V*), XE1474 (*dat-1p::rde-1::SL2::sid-1 + unc-119(+); wpSi6 II; eri-1(mg366) IV; rde-1(ne219) V; lin-15B(n744) X*).

The following strains were made in our laboratory previously and used in this study:

PMD13 (*rrf-3(b26) II; fem-1(hc17) IV; egl-1[dat-1p::GFP]*)³⁶

PMD249 (*utsEx19 [dat-1p::ORP1::roGFP2::T2A::mCherry::unc-54 3' UTR]; wpSi6 [dat-1p::rde-1::SL2::sid-1 + unc-119(+)] II; eri-1(mg366) IV; rde-1(ne219) V; lin-15B(n744) X*)¹¹

PMD216 (*fem-1(hc17) IV, rrf-3(b26) II; egl-1[dat-1p::GFP]; dat-1p::rde-1::SL2::sid-1 + unc-119(+); wpSi6 II; eri-1(mg366) IV; rde-1(ne219) V; lin-15B(n744) X*)¹¹

RDE-1 and SID-1 mutants were always confirmed by feeding of *cdc-25.1* RNAi which creates sterile animals when there is functional RDE-1 in the germline. Transgenic rescue of RDE-1 or SID-1 expression in the tissue of interest was confirmed using GFP RNAi.

C. elegans trauma

Trauma was induced in *C. elegans* using our mechanical stress agitation model as described here³⁶. Age-synchronized worms were grown on either empty vector control (EV) or the respective RNAi. Temperature-restrictive strains were maintained at 25 °C to prevent progeny generation. On the first day of adulthood, worms were rinsed off growth plates in liquid M9 buffer and centrifuged at 1000 × g for 30 s to pellet them. A 125 µl volume of worm pellets was transferred to 2 ml Precellys tubes (Thermo Fisher Scientific 02-682-556) and M9 buffer was added to make up a total volume of 500 µl. The worms were then subjected to high-frequency, multidirectional agitation in a Precellys Evolution homogenizer (Bertin Instruments P000062-PEVO0-A.0) for 16 s at 8600 rpm. After agitation, the worms were pelleted at 1000 × g for 30 s and transferred to fresh recovery plates containing the same RNAi or EV they were grown on before trauma. Control worms, which were not injured, were suspended in M9 for the same duration and then transferred to recovery plates without trauma.

Large particle flow cytometry

Worms were analyzed using the COPAS FP-250 large particle flow cytometer (Union Biometrica) along with the LP Sampler (Union Biometrica) to automate sample acquisition. Worms were washed off 100 mm plates with M9 and rinsed three times with M9 before 100 µl worm pellets were loaded into a 96-well plate for acquisition. To prevent cross-well contamination, M9 was loaded into wells between samples. COPAS GP SHEATH REAGENT (Union Biometrica 300-5070-100) was used as the flow sheath solution. Extinction was measured using a 488 nm laser and a 1.3 neutral density filter for all experiments, except for ROS sensor (PMD249) measurements, which utilized a 561 nm laser and a 2.0 neutral density filter to allow 405 nm measurements without any 488 nm excitation. Laser power and PMT voltage were empirically optimized for each strain and maintained consistently for each experiment. The gain setting was always set at 1.0 for extinction and 2.0 for all fluorescent channels. Data was collected and processed using Union Biometrica FlowPilot software (version 1.6.1.8) and further normalized in Excel (Microsoft).

Dopaminergic GFP index

To compare the delta dopaminergic GFP retention between EV and RNAi conditions, peak height GFP was normalized as described previously³⁶. Briefly, the GFP retention of individual injured worms was calculated by dividing the GFP peak height value by the average GFP peak height value of uninjured controls from the corresponding genotype or RNAi condition. These GFP retention percentages were then normalized to WT or EV controls using the formula below. As a result, any positive value can be interpreted as protective while any negative value can be interpreted as degenerative compared to control conditions. The resulting product is referred to as the

Dopaminergic GFP index.

$$\text{Dopaminergic GFP index} = \frac{(\text{control GFP retention}\Delta - \text{test GFP retention}\Delta)}{(\text{control GFP retention}\Delta - 1)} \quad (1)$$

Oxidation ratio

Oxidation ratio was calculated as described previously¹¹. Briefly, background fluorescence was accounted for by subtracting the mean GFP fluorescence obtained from the mCherry- population from the mCherry+ population. This background normalized 405/488 ratio from the injured population was then normalized to time-matched, uninjured controls via subtraction of the average uninjured, blank normalized, 405/488 ratio.

$$\text{Oxidation ratio} = \frac{\text{Injured} \left(\frac{405 \text{ mCh}^+ - \text{mean } 405 \text{ mCh}^-}{\text{mean } 488 \text{ mCh}^+ - \text{mean } 488 \text{ mCh}^-} \right) - \text{mean uninjured} \left(\frac{405 \text{ mCh}^+ - \text{mean } 405 \text{ mCh}^-}{\text{mean } 488 \text{ mCh}^+ - \text{mean } 488 \text{ mCh}^-} \right)}{(2)}$$

RNAi Administration

Worm strains were grown on HT115 *E. coli* expressing RNAi constructs from either the Ahringer⁷⁵ or Vidal RNAi libraries⁷⁶. The L4440 empty vector control (EV) RNAi construct was used for control treatments. RNAi strains were grown in small starter cultures before inoculating larger cultures in Terrific Broth (TB) containing carbenicillin, and grown for 15 h on an orbital shaker at 37 °C. After 15 h, cultures were induced with 1 mM IPTG and incubated for an additional 4 h at 37 °C to ensure RNAi expression. Cultures were then centrifuged at 4000 × g for 10 min and bacterial pellets were re-suspended in 1/5th of the original culture volume in TB before being spread on 100 mm NGM plates containing a final concentration of 1 mM IPTG and 0.1 mg/ml carbenicillin. When combining multiple RNAi constructs on one plate, cultures were mixed by volume prior to seeding. All RNAi constructs used are listed in Supplementary Table S2.

CUT&RUN

CUT&RUN experiments were performed using the CUT&RUN Assay Kit (Cell Signaling Technology 86652) following manufacturers recommendations. Differentiated LUHMES cells were treated with 10 nM TG or DMSO and collected 24 h later. Cells were lifted via trypsinization, and triplicate conditions were mixed and counted. All following steps were done in duplicate where each duplicate was a pool of 3 separate replicates. Per sample 100,000 cells were aliquoted and washed two times using 1x wash buffer (+ spermidine and protease inhibitor cocktail). Cells were then immobilized with concanavalin A beads and incubated overnight at 4 °C with the primary antibody at a 1:50 dilution for both anti-H3K4me3 (Cell Signaling Technology C42D8) and anti-YY1 (Cell Signaling Technology D5D9Z). The following day, pAG-MNase mixture was added and incubated at 4 °C for 1 hour. After 3 washes with digitonin wash buffer cells were cooled on ice for 5 min and pAG-MNase was activated with cold calcium chloride and incubated at 4 °C for 30 min. 1x stop buffer was added and diffused DNA-samples were purified using DNA spin columns. Input samples were prepared via sonication using 6 × 15 s pulses with 30 s pauses. Input fragment size of ~300–400 bp was confirmed using agarose gel electrophoresis. Enriched DNA samples were then submitted for library prep and paired-end sequencing done by Novogene (Sacramento, CA).

G4 CUT&RUN was performed on cells treated with 10 nM TG or DMSO collected 24 h later. 6 biological replicates per condition were all trypsinized, counted, and pooled together prior to the CUT&RUN assay (250,000 cells per sample). Experimental samples were

incubated overnight at 4 °C with BG4 primary antibody (Millipore Sigma MABE917) at a 1:50 dilution. The next day, the primary BG4 antibody was removed, cells were washed once using digitonin wash buffer, and the anti-FLAG secondary antibody (Sigma Aldrich F1804) was added at a 1:100 dilution for 1 h at room temperature. Control samples that were not incubated with the BG4 primary received anti-FLAG only. The remaining steps were performed the same as described above.

FASTQ files of the raw sequencing results were then uploaded to Galaxy and trimmed using TRIMMOMATIC 0.38.1 and the following command: ILLUMINACLIP:/usr/local/share/trimmomatic-0.38.1/adapters/TruSeq2-PE.fa:2:15:4:4:true LEADING:20 TRAILING:20 SLIDINGWINDOW:4:15 MINLEN:25. Trimmed reads were then mapped to human genome hg38 using Bowtie2 and the following command: bowtie2 -local -very-fast-local -no-unal -hg38 -no-mixed -no-discordant -110 -X 500. Alignment BAM files were then sorted and merged with their duplicate using Samtools. Bigwig coverage files were then generated using bamCoverage (deeptools⁷⁷ 3.5.1) and normalized to each other using counts per million.

YY1 peak calling was performed using MACS2⁷⁸ (version 2.2.7.1) with a Minimum FDR q-value cutoff for peak detection set at 0.05. DMSO and TG treated input reads were used as a background ChIP-seq control. Following MACS2 peak calling, any regions with a ≥ 1 bp overlap with blacklisted regions (ENCF356LFX) or any regions that were called in the input file were subtracted from the YY1 regions using bedtools SubtractBed. Profiles and heatmaps of peak regions were generated using Deeptools⁷⁷ (version 3.5.1) computeMatrix and plotHeatmap functions. Any further annotations of genomic regions overlapping with YY1 bound regions were performed using Bioconductor ChIPseeker⁷⁹ (version 1.18.0).

BG4 peak calling was performed in the same fashion with the exception of using DMSO or TG treated anti-FLAG only as background controls.

Read counts per region were calculated using Deeptools plotEnrichment and normalized to total reads per samples. All regions were scaled to the same size (1 kb) to allow for direct comparison.

Circular dichroism

Single stranded DNA probes were synthesized and HPLC purified by Integrated DNA Technologies. The day before CD spectra acquisition, probes were resuspended at 10 μM in folding buffer (20 mM Tris-HCl and 50 mM KCl, pH 7.4), heated at 95 °C for 10 min to unfold prior secondary structures and gradually cooled overnight at RT to allow refolding. CD spectra were acquired at room temperature at the wavelength range of 220 to 320 nm using a Jasco J-815 Circular Dichroism Spectrometer. Spectra were acquired at 1 nm bandwidth interval and 10 accumulations were collected for each probe. CD melt curves were subsequently collected between 20 and 95 °C at a heating rate of 1 °C/min and measuring ellipticity at 242 nm and 263 nm every degree increased. TMPyP₄ and recombinant YY1 (Prospec) were spiked in prior to CD acquisition at 10 μM and 500 nM respectively.

in vitro G4 polymerase inhibition assay

Semi-quantitative G4 PCRs were performed using either a standard Taq polymerase (Qiagen) or a high fidelity Q5 polymerase (NEB). Briefly, a universal master mix containing primers, nucleotides, polymerase, and PCR buffer was split into three and linearized plasmid constructs were spiked in (TH cDNA, TH + 6, or TH + 10) with or without the addition of TMPyP₄. PCR was carried out for 20 cycles and amplification products were assessed using agarose gel electrophoresis.

in vivo G4 inhibition assay

HEK293t cells were seeded in a 96 well plate at 20,000 cells per well one day prior to transfection. DNA constructs (CMV::TH + 6-mCherry

and CMV::TH + 10-mCherry) were transfected with jetPRIME (Polyplus Sartorius) at a DNA concentration of 100 ng per well with a DNA to jetPRIME ratio of 1:2. 30 min post-transfection TMPyP4 was added at a concentration range of 0, 312.5, 625, 1250, 2500, 5000 nM. mCherry production was then monitored using CLARIOstar temperature and atmosphere controlled fluorescent plate reader (BMG Labtech).

Statistical analysis

All statistical analyses were conducted using GraphPad Prism (version 9.5.0) and Qiagen Bioinformatics CLC Genomics Workbench (version 9.5). For large worm populations, outliers were removed using the ROUT method (Q = 1%) prior to analysis.

Reporting summary

Further information on research design is available in the Nature Portfolio Reporting Summary linked to this article.

Data availability

All transcriptomic and CUT&RUN datasets generated during this study are deposited in the NCBI Gene Expression Omnibus (GEO) under the accession number [GSE254193](https://www.ncbi.nlm.nih.gov/geo/query/acc.cgi?acc=GSE254193) (<https://www.ncbi.nlm.nih.gov/geo/query/acc.cgi?acc=GSE254193>).

The raw data generated in this study and expanded details on the statistical tests used are provided in the Supplementary Information and Source Data file. Any additional information is available from the corresponding author upon request. Source data are provided with this paper.

References

- Nikolaus, S., Antke, C. & Muller, H. W. In vivo imaging of synaptic function in the central nervous system: II. Mental and affective disorders. *Behav. Brain Res.* **204**, 32–66 (2009).
- Tang, T. S. et al. Huntingtin and huntingtin-associated protein 1 influence neuronal calcium signaling mediated by inositol-(1,4,5) triphosphate receptor type 1. *Neuron* **39**, 227–239 (2003).
- Hartley, D. M. et al. Protofibrillar intermediates of amyloid beta-protein induce acute electrophysiological changes and progressive neurotoxicity in cortical neurons. *J. Neurosci.* **19**, 8876–8884 (1999).
- Kamenetz, F. et al. APP processing and synaptic function. *Neuron* **37**, 925–937 (2003).
- Heo, J. Y. et al. Aberrant tonic inhibition of dopaminergic neuronal activity causes motor symptoms in animal models of Parkinson's disease. *Curr. Biol.* **30**, 276–291.e279 (2020).
- Surmeier, D. J., Obeso, J. A. & Halliday, G. M. Selective neuronal vulnerability in Parkinson disease. *Nat. Rev. Neurosci.* **18**, 101–113 (2017).
- LaVoie, M. J., Ostaszewski, B. L., Weihofen, A., Schlossmacher, M. G. & Selkoe, D. J. Dopamine covalently modifies and functionally inactivates parkin. *Nat. Med.* **11**, 1214–1221 (2005).
- Mosharov, E. V. et al. Interplay between cytosolic dopamine, calcium, and alpha-synuclein causes selective death of substantia nigra neurons. *Neuron* **62**, 218–229 (2009).
- Tse, D. C., McCreery, R. L. & Adams, R. N. Potential oxidative pathways of brain catecholamines. *J. Med. Chem.* **19**, 37–40 (1976).
- Hastings, T. G., Lewis, D. A. & Zigmond, M. J. Role of oxidation in the neurotoxic effects of intrastriatal dopamine injections. *Proc. Natl Acad. Sci. USA* **93**, 1956–1961 (1996).
- Zuurbier, K. R. et al. Cytosolic dopamine determines hypersensitivity to blunt force trauma. *iScience* **27**, 110094 (2024).
- Abe, M. et al. Effects of 1-cyclohexyl- and 1-cyclohexyl-N-propargyl-1,2,3,4-tetrahydroisoquinoline on dopaminergic spontaneous discharge in nigral neurons of rats. *Brain Res Bull.* **121**, 201–208 (2016).
- Chang, X., Ma, Z., Shi, L. & Xie, J. Effects of ghrelin on the electrical activities of substantia nigra dopaminergic neurons treated with MPP. *Neurochem Int* **138**, 104780 (2020).
- Good, C. H. et al. Impaired nigrostriatal function precedes behavioral deficits in a genetic mitochondrial model of Parkinson's disease. *FASEB J.* **25**, 1333–1344 (2011).
- Gonzalez-Rodriguez, P. et al. Disruption of mitochondrial complex I induces progressive parkinsonism. *Nature* **599**, 650–656 (2021).
- Janezic, S. et al. Deficits in dopaminergic transmission precede neuron loss and dysfunction in a new Parkinson model. *Proc. Natl Acad. Sci. USA* **110**, E4016–E4025 (2013).
- Tozzi, A. et al. Dopamine-dependent early synaptic and motor dysfunctions induced by alpha-synuclein in the nigrostriatal circuit. *Brain* **144**, 3477–3491 (2021).
- Chou, J. S. et al. G2019S LRRK2 causes early-phase dysfunction of SNpc dopaminergic neurons and impairment of corticostriatal long-term depression in the PD transgenic mouse. *Neurobiol Dis* **68**, 190–199 (2014).
- Lotharius, J. et al. Effect of mutant alpha-synuclein on dopamine homeostasis in a new human mesencephalic cell line. *J. Biol. Chem.* **277**, 38884–38894 (2002).
- Kaneko, Y. & Tsukamoto, A. Thapsigargin-induced persistent intracellular calcium pool depletion and apoptosis in human hepatoma cells. *Cancer Lett.* **79**, 147–155 (1994).
- Li, L. & Hu, G. K. Pink1 protects cortical neurons from thapsigargin-induced oxidative stress and neuronal apoptosis. *Biosci. Rep.* **35**, <https://doi.org/10.1042/BSR20140104> (2015).
- Scheper, W. & Hoozemans, J. J. Endoplasmic reticulum protein quality control in neurodegenerative disease: the good, the bad and the therapy. *Curr. Med. Chem.* **16**, 615–626 (2009).
- Chen, X. Y., Liu, C., Xue, Y. & Chen, L. Changed firing activity of nigra dopaminergic neurons in Parkinson's disease. *Neurochem. Int.* **162**, 105465 (2023).
- Crawford, D. C. & Mennerick, S. Presynaptically silent synapses: dormancy and awakening of presynaptic vesicle release. *Neuroscientist* **18**, 216–223 (2012).
- Welch, G. M. et al. Neurons burdened by DNA double-strand breaks incite microglia activation through antiviral-like signaling in neurodegeneration. *Sci. Adv.* **8**, eabo4662 (2022).
- Lu, T. et al. REST and stress resistance in ageing and Alzheimer's disease. *Nature* **507**, 448–454 (2014).
- Pifl, C. et al. Is Parkinson's disease a vesicular dopamine storage disorder? Evidence from a study in isolated synaptic vesicles of human and nonhuman primate striatum. *J. Neurosci.* **34**, 8210–8218 (2014).
- Uhl, G. R. Dopamine compartmentalization, selective dopaminergic vulnerabilities in Parkinson's disease and therapeutic opportunities. *Ann. Clin. Transl. Neurol.* **6**, 406–415 (2019).
- Bucher, M. L. et al. Acquired dysregulation of dopamine homeostasis reproduces features of Parkinson's disease. *NPJ Parkinsons Dis.* **6**, 34 (2020).
- Ford, C. P. The role of D2-autoreceptors in regulating dopamine neuron activity and transmission. *Neuroscience* **282**, 13–22 (2014).
- Kuo, S. C. & Lampen, J. O. Tunicamycin—an inhibitor of yeast glycoprotein synthesis. *Biochem Biophys. Res. Commun.* **58**, 287–295 (1974).
- Liu, G. H. et al. Progressive degeneration of human neural stem cells caused by pathogenic LRRK2. *Nature* **491**, 603–607 (2012).
- Fiore, N. J., Tamer-Mahoney, J. D., Beheshti, A., Nieland, T. J. F. & Kaplan, D. L. 3D biocomposite culture enhances differentiation of dopamine-like neurons from SH-SY5Y cells: A model for studying Parkinson's disease phenotypes. *Biomaterials* **290**, 121858 (2022).
- Solano Fonseca, R. et al. Glycolytic preconditioning in astrocytes mitigates trauma-induced neurodegeneration. *Elife* **10**, <https://doi.org/10.7554/eLife.69438> (2021).
- Sulston, J., Dew, M. & Brenner, S. Dopaminergic neurons in the nematode *Caenorhabditis elegans*. *J. Comp. Neurol.* **163**, 215–226 (1975).

36. Egge, N. et al. Trauma-induced regulation of VHP-1 modulates the cellular response to mechanical stress. *Nat. Commun.* **12**, 1484 (2021).
37. Nass, R., Hall, D. H., Miller, D. M. 3rd & Blakely, R. D. Neurotoxin-induced degeneration of dopamine neurons in *Caenorhabditis elegans*. *Proc. Natl Acad. Sci. USA* **99**, 3264–3269 (2002).
38. Gordon, S., Akopyan, G., Garban, H. & Bonavida, B. Transcription factor YY1: structure, function, and therapeutic implications in cancer biology. *Oncogene* **25**, 1125–1142 (2006).
39. Sarvagalla, S., Kolapalli, S. P. & Vallabhapurapu, S. The Two Sides of YY1 in Cancer: A Friend and a Foe. *Front Oncol.* **9**, 1230 (2019).
40. Wang, Y. et al. Yin Yang 1 promotes the Warburg effect and tumorigenesis via glucose transporter GLUT3. *Cancer Sci.* **109**, 2423–2434 (2018).
41. Park, A. et al. Identification of Transcription Factor YY1 as a Regulator of a Prostate Cancer-Specific Pathway Using Proteomic Analysis. *J. Cancer* **8**, 2303–2311 (2017).
42. Seto, E., Shi, Y. & Shenk, T. YY1 is an initiator sequence-binding protein that directs and activates transcription in vitro. *Nature* **354**, 241–245 (1991).
43. Shi, Y., Seto, E., Chang, L. S. & Shenk, T. Transcriptional repression by YY1, a human GLI-Kruppel-related protein, and relief of repression by adenovirus E1A protein. *Cell* **67**, 377–388 (1991).
44. Donohoe, M. E., Zhang, L. F., Xu, N., Shi, Y. & Lee, J. T. Identification of a Ctf cofactor, Yy1, for the X chromosome binary switch. *Mol. Cell* **25**, 43–56 (2007).
45. Weintraub, A. S. et al. YY1 Is a Structural Regulator of Enhancer-Promoter Loops. *Cell* **171**, 1573–1588.e1528 (2017).
46. Fishilevich, S. et al. GeneHancer: genome-wide integration of enhancers and target genes in GeneCards. *Database (Oxford)* **2017**, <https://doi.org/10.1093/database/bax028> (2017).
47. Li, L. et al. YY1 interacts with guanine quadruplexes to regulate DNA looping and gene expression. *Nat. Chem. Biol.* **17**, 161–168 (2021).
48. Tikhonova, P. et al. DNA G-Quadruplexes Contribute to CTCF Recruitment. *Int. J. Mol. Sci.* **22**, <https://doi.org/10.3390/ijms22137090> (2021).
49. Roychoudhury, S. et al. Endogenous oxidized DNA bases and APE1 regulate the formation of G-quadruplex structures in the genome. *Proc. Natl Acad. Sci. USA* **117**, 11409–11420 (2020).
50. Hansel-Hertsch, R. et al. G-quadruplex structures mark human regulatory chromatin. *Nat. Genet.* **48**, 1267–1272 (2016).
51. Cagirici, H. B., Budak, H. & Sen, T. Z. G4Boost: a machine learning-based tool for quadruplex identification and stability prediction. *BMC Bioinforma.* **23**, 240 (2022).
52. Brazda, V. et al. G4Hunter web application: a web server for G-quadruplex prediction. *Bioinformatics* **35**, 3493–3495 (2019).
53. Li, C. et al. Ligand-induced native G-quadruplex stabilization impairs transcription initiation. *Genome Res.* **31**, 1546–1560 (2021).
54. Gorini, F. et al. The genomic landscape of 8-oxodG reveals enrichment at specific inherently fragile promoters. *Nucleic Acids Res.* **48**, 4309–4324 (2020).
55. Rogakou, E. P., Boon, C., Redon, C. & Bonner, W. M. Megabase chromatin domains involved in DNA double-strand breaks in vivo. *J. Cell Biol.* **146**, 905–916 (1999).
56. Jackson, S. P. & Bartek, J. The DNA-damage response in human biology and disease. *Nature* **461**, 1071–1078 (2009).
57. Casper, A. M., Nghiem, P., Arlt, M. F. & Glover, T. W. ATR regulates fragile site stability. *Cell* **111**, 779–789 (2002).
58. Varshney, D., Spiegel, J., Zyner, K., Tannahill, D. & Balasubramanian, S. The regulation and functions of DNA and RNA G-quadruplexes. *Nat. Rev. Mol. Cell Biol.* **21**, 459–474 (2020).
59. Ambrus, A., Chen, D., Dai, J., Jones, R. A. & Yang, D. Solution structure of the biologically relevant G-quadruplex element in the human c-MYC promoter. Implications for G-quadruplex stabilization. *Biochemistry* **44**, 2048–2058 (2005).
60. Belotserkovskii, B. P. et al. Mechanisms and implications of transcription blockage by guanine-rich DNA sequences. *Proc. Natl Acad. Sci. USA* **107**, 12816–12821 (2010).
61. Broxson, C., Beckett, J. & Tornaletti, S. Transcription arrest by a G quadruplex forming-trinucleotide repeat sequence from the human c-myc gene. *Biochemistry* **50**, 4162–4172 (2011).
62. Zheng, K. W. et al. Co-transcriptional formation of DNA:RNA hybrid G-quadruplex and potential function as constitutional cis element for transcription control. *Nucleic Acids Res.* **41**, 5533–5541 (2013).
63. Hiromura, M. et al. YY1 is regulated by O-linked N-acetylglucosaminylation (O-glcNAcylation). *J. Biol. Chem.* **278**, 14046–14052 (2003).
64. Zhang, W. J. et al. Regulation of Transcription Factor Yin Yang 1 by SET7/9-mediated Lysine Methylation. *Sci. Rep.* **6**, 21718 (2016).
65. Walowitz, J. L., Bradley, M. E., Chen, S. & Lee, T. Proteolytic regulation of the zinc finger transcription factor YY1, a repressor of muscle-restricted gene expression. *J. Biol. Chem.* **273**, 6656–6661 (1998).
66. Yao, Y. L., Yang, W. M. & Seto, E. Regulation of transcription factor YY1 by acetylation and deacetylation. *Mol. Cell Biol.* **21**, 5979–5991 (2001).
67. Griesenbeck, J., Ziegler, M., Tomilin, N., Schweiger, M. & Oei, S. L. Stimulation of the catalytic activity of poly(ADP-ribosyl) transferase by transcription factor Yin Yang 1. *FEBS Lett.* **443**, 20–24 (1999).
68. Oei, S. L. et al. Interaction of the transcription factor YY1 with human poly(ADP-ribosyl) transferase. *Biochem Biophys. Res Commun.* **240**, 108–111 (1997).
69. Oei, S. L. & Shi, Y. Poly(ADP-ribosyl)ation of transcription factor Yin Yang 1 under conditions of DNA damage. *Biochem Biophys. Res Commun.* **285**, 27–31 (2001).
70. Deng, Z., Wan, M. & Sui, G. PIASy-mediated sumoylation of Yin Yang 1 depends on their interaction but not the RING finger. *Mol. Cell Biol.* **27**, 3780–3792 (2007).
71. Hongo, F. et al. Inhibition of the transcription factor Yin Yang 1 activity by S-nitrosation. *Biochem Biophys. Res Commun.* **336**, 692–701 (2005).
72. Rizkallah, R. & Hurt, M. M. Regulation of the transcription factor YY1 in mitosis through phosphorylation of its DNA-binding domain. *Mol. Biol. Cell* **20**, 4766–4776 (2009).
73. Zachara, N. E. et al. Dynamic O-GlcNAc modification of nucleocytoplasmic proteins in response to stress. A survival response of mammalian cells. *J. Biol. Chem.* **279**, 30133–30142 (2004).
74. Krippner-Heidenreich, A. et al. Caspase-dependent regulation and subcellular redistribution of the transcriptional modulator YY1 during apoptosis. *Mol. Cell Biol.* **25**, 3704–3714 (2005).
75. Kamath, R. S. et al. Systematic functional analysis of the *Caenorhabditis elegans* genome using RNAi. *Nature* **421**, 231–237 (2003).
76. Rual, J. F. et al. Toward improving *Caenorhabditis elegans* phenome mapping with an ORFeome-based RNAi library. *Genome Res.* **14**, 2162–2168 (2004).
77. Ramirez, F. et al. deepTools2: a next generation web server for deep-sequencing data analysis. *Nucleic Acids Res.* **44**, W160–W165 (2016).
78. Zhang, Y. et al. Model-based analysis of ChIP-Seq (MACS). *Genome Biol.* **9**, R137 (2008).
79. Yu, G., Wang, L. G. & He, Q. Y. ChIPseeker: an R/Bioconductor package for ChIP peak annotation, comparison and visualization. *Bioinformatics* **31**, 2382–2383 (2015).

Acknowledgements

We appreciate the *Caenorhabditis* Genetics Center (CGC) for worm strains. We thank Dr. Michael Douglas for their critical review of the manuscript. This work has been funded by the Clayton Foundation for Research, the Welch Foundation (I-2061-20210327), the NIH

(R01AG076529, R01AG061338, and 5F31GM140620), the American Federation for Aging Research/Hevolution, the National Science Foundation (NSF GRFP 1000305318), and the UT Southwestern Peter O'Donnell Jr. Brain Institute Neural Scientist Training Program.

Author contributions

Conceptualization: K.R.Z., P.M.D.; Methodology: K.R.Z., S.L.B.A., R.S.F., S.B., L.M.T., G.O., P.M., P.M.D.; Investigation: K.R.Z., S.L.B.A., R.S.F., L.M.T., P.M., J.M.W., J.K. Visualization: K.R.Z., P.M.D.; Funding acquisition: K.R.Z., L.M.T., P.M.D.; Project administration: K.R.Z.; Supervision: P.M.D.; Writing – original draft: K.R.Z., P.M.D.; Writing – review & editing: K.R.Z., R.S.F., P.M.D.

Competing interests

The authors declare no competing interests.

Additional information

Supplementary information The online version contains supplementary material available at <https://doi.org/10.1038/s41467-024-54958-9>.

Correspondence and requests for materials should be addressed to Peter M. Douglas.

Peer review information *Nature Communications* thanks Cynthia McMurray and the other, anonymous, reviewer(s) for their contribution to the peer review of this work. A peer review file is available.

Reprints and permissions information is available at <http://www.nature.com/reprints>

Publisher's note Springer Nature remains neutral with regard to jurisdictional claims in published maps and institutional affiliations.

Open Access This article is licensed under a Creative Commons Attribution-NonCommercial-NoDerivatives 4.0 International License, which permits any non-commercial use, sharing, distribution and reproduction in any medium or format, as long as you give appropriate credit to the original author(s) and the source, provide a link to the Creative Commons licence, and indicate if you modified the licensed material. You do not have permission under this licence to share adapted material derived from this article or parts of it. The images or other third party material in this article are included in the article's Creative Commons licence, unless indicated otherwise in a credit line to the material. If material is not included in the article's Creative Commons licence and your intended use is not permitted by statutory regulation or exceeds the permitted use, you will need to obtain permission directly from the copyright holder. To view a copy of this licence, visit <http://creativecommons.org/licenses/by-nc-nd/4.0/>.

© The Author(s) 2024